



RESEARCH ARTICLE

10.1029/2024MS004321

Key Points:

- Numerical mixing due to the discretization of tracer advection is quantified for three advection schemes in idealized numerical simulations
- Mixing in frontal zones is dominated by numerical mixing even at submesoscale-resolving resolutions
- Comparison across different advection schemes suggests increased numerical mixing alters the large scale circulation and tracer state

Supporting Information:

Supporting Information may be found in the online version of this article.

Correspondence to:

D. Schlichting,
dschlichting@lanl.gov

Citation:

Schlichting, D., Hetland, R., & Jones, C. S. (2024). Numerical mixing suppresses submesoscale baroclinic instabilities over sloping bathymetry. *Journal of Advances in Modeling Earth Systems*, 16, e2024MS004321. <https://doi.org/10.1029/2024MS004321>

Received 2 MAR 2024

Accepted 14 OCT 2024

Numerical Mixing Suppresses Submesoscale Baroclinic Instabilities Over Sloping Bathymetry

Dylan Schlichting^{1,2} , Robert Hetland³ , and C. Spencer Jones¹

¹Department of Oceanography, Texas A&M University, College Station, TX, USA, ²Los Alamos National Laboratory, Los Alamos, NM, USA, ³Pacific Northwest National Laboratory, Richland, WA, USA

Abstract The impacts of spurious numerical salinity mixing (\mathcal{M}_{num}) on the larger-scale flow and tracer fields are characterized using idealized simulations. The idealized model is motivated by realistic simulations of the Texas-Louisiana shelf and features oscillatory near-inertial wind forcing. \mathcal{M}_{num} can exceed the physical mixing from the turbulence closure (\mathcal{M}_{phy}) in frontal zones and within the mixed layer. This suggests that simulated mixing processes in frontal zones are driven largely by \mathcal{M}_{num} . Near-inertial alongshore wind stress amplitude is varied to identify a base case that maximizes the ratio of \mathcal{M}_{num} to \mathcal{M}_{phy} in simulations with no prescribed horizontal mixing. We then test the sensitivity of the base case with three tracer advection schemes (MPDATA, U3HC4, and HSIMT) and conduct ensemble runs with perturbed bathymetry. Instability growth is evaluated using the volume-integrated eddy kinetic energy (*EKE*) and available potential energy (*APE*). While all schemes have similar total mixing, the HSIMT simulations have over double the volume-integrated \mathcal{M}_{num} and 20% less \mathcal{M}_{phy} relative to other schemes, which suppresses the release of *APE* and reduces the *EKE* by roughly 25%. This results in reduced isohaline variability and steeper isopycnals, evidence that enhanced \mathcal{M}_{num} suppresses instability growth. Differences in *EKE* and *APE* between the MPDATA and U3HC4 simulations are marginal. However, the U3HC4 simulations have 25% more \mathcal{M}_{num} . Experiments with variable horizontal viscosity and diffusivity coefficients show that small amounts of prescribed horizontal mixing improve the representation of the ocean state for all advection schemes by reducing the \mathcal{M}_{num} and increasing the *EKE*.

Plain Language Summary Mixing plays a fundamental role in maintaining the general circulation of the ocean by dissipating energy and redistributing tracers, or fluid properties used to track aspects of ocean circulation. Numerical ocean models often parameterize physical mixing processes because their resolution is too coarse to resolve them. Numerical models are also prone to numerical mixing, a type of spurious mixing arising from the discretization of tracer transport by currents. Recent studies have shown numerical mixing can exceed the physical mixing in high resolution models. Here, we study where numerical salinity mixing is significant in the water column and how it impacts the larger-scale circulation and tracer fields in a 500 m resolution idealized model of the Texas-Louisiana shelf. We find that numerical mixing dominates physical mixing in frontal zones associated with small-scale eddies. To study the impacts of that mixing, we perform an ensemble by varying the numerical scheme for tracer transport. We find that the scheme with excessive numerical mixing suppresses the eddies and prevents the release of their primary energy source. Future studies may use these results as a blueprint to better understand how numerical mixing impacts specific processes near frontal zones and therefore affects model fidelity.

1. Introduction

Mixing, or the irreversible loss of scalar variance by turbulent processes, is a fundamental ocean process because it redistributes tracers and dissipates energy. Recent studies have focused on characterizing numerical mixing—defined as the spurious mixing generated by the discretization of tracer advection—because it can be a significant fraction of, or even exceed, the physical mixing. Physical mixing is defined in this study as the destruction of tracer variance prescribed by turbulence closure schemes (Burchard & Rennau, 2008; MacCready et al., 2018), whereas numerical mixing is generally associated with the imperfect discretization of tracer advection. Significant numerical mixing relative to physical mixing has been demonstrated for high-resolution estuarine models (Ralston et al., 2017; Rennau & Burchard, 2009; Wang et al., 2021), submesoscale eddy-resolving regional models (Schlichting et al., 2023), and a wide range of global models (Griffies et al., 2000; Holmes et al., 2021; Illicak et al., 2012; Megann, 2018).

It has been known for decades that spurious mixing can degrade the fidelity of numerical ocean models, driving the model toward unrealistic ocean states. A prominent early example of this was discovered by George Veronis, who showed that the Laplacian diffusion implemented in an ocean circulation model caused unphysical upwelling in western boundary currents (Veronis, 1975). The problem resulted from the misalignment of the diffusion tensor and isopycnals, which aliased the prescribed horizontal diffusion as diapycnal diffusion over steeply sloped isopycnals and caused false upwelling near western boundary currents (Griffies et al., 2000). The “Veronis effect” was not mitigated until ocean models employed a rotated diffusion tensor to minimize spurious diapycnal mixing (Redi, 1982). Numerical mixing is one source of spurious mixing; there are several others in modern ocean models (see Megann et al., 2022).

Unlike physical mixing, numerical mixing is not easily controlled by model parameters. This is because numerical mixing is sensitive to components of the model setup such as the momentum advection scheme (Ilicak et al., 2012), tracer advection scheme (Fofanova et al., 2021; Kalra et al., 2019; Wang et al., 2021), and grid resolution (Holmes et al., 2021; Ralston et al., 2017; Schlichting et al., 2023). It also depends on the resolved flow velocity and tracer gradients (Holmes et al., 2021; Schlichting et al., 2023; Wang et al., 2021). Numerical mixing can be negative for advection schemes that attempt to reduce diffusion (e.g., flux-corrected or flux-limited schemes). In this case, tracers may be redistributed up-gradient and spuriously create grid-scale tracer variance. The nonlinear nature of the problem makes it difficult to quantify the larger-scale impacts of numerical mixing without targeted numerical experiments (Fofanova et al., 2021; Kalra et al., 2019; Mohammadi-Aragh et al., 2015). However, it is generally thought that numerical mixing impacts the larger-scale flow and tracer fields differently than the physical mixing in primitive equation models.

Although numerical mixing is a source of error in coarse-resolution simulations, it can be used to eliminate grid-scale kinetic energy and tracer variance in high-resolution simulations. For example, odd-ordered advection schemes that are numerically dissipative are commonly used in coastal and large eddy simulation (LES) applications (Leonard et al., 1993; Roman et al., 2010; Shchepetkin & McWilliams, 1998). In these simulations, numerical mixing can be used to improve model stability and fidelity by removing energy at the grid-scale. Without this numerical mixing, energy that cascades from large to small scales would gather at the grid-scale, dominating the solution and creating an unphysical ocean state.

In implicit LES models, part of the turbulence cascade is resolved and implicit numerical dissipation is included into the discretization of the momentum equations instead of using a subgrid-scale model to represent the unresolved motions (Dairay et al., 2017; Domaradzki et al., 2003; Grinstein et al., 2007; Thornber et al., 2007). In other words, the effects of numerical mixing are used to mimic physical mixing. For example, Dairay et al. (2017) found better representation of the Taylor-Green vortex problem when using artificial numerical dissipation (included into the discretization of the viscous term of the momentum equations) without a subgrid-scale model compared to simulations that used the Smagorinsky (1963) model.

Numerical mixing decreases the accuracy of very high-resolution primitive equation ocean models capable of permitting or resolving submesoscale processes (Henell et al., 2023; Mohammadi-Aragh et al., 2015). Submesoscales are characterized by $\mathcal{O}(1)$ Rossby and Richardson numbers, a dual cascade of energy, and large vertical motions (McWilliams, 2016; Taylor & Thompson, 2023). Thus, we expect there to be substantial differences in the character of numerical mixing in submesoscale-resolving models compared to those that resolve only mesoscale flows. Submesoscales are important for many oceanographic processes, for example, (a) they restratify the mixed layer and thus play an important role in structuring the ocean's heat budget (Boccaletti et al., 2007; Su et al., 2018), (b) their ageostrophic motions can create a ventilation pathway for bottom trapped material (Qu, Thomas, Wienkers, et al., 2022) and exchange tracers across the mixed layer base (Balwada et al., 2018, 2021), and (c) their convergent motions (i.e., fronts) congregate marine organisms and biogenic surfactants (McWilliams, 2019; Ruiz et al., 2019). Therefore, it is critical to understand and quantify numerical mixing at sub-kilometer scales as regional coastal models and limited domain open ocean models push toward submesoscale-resolving resolutions.

Mohammadi-Aragh et al. (2015) examined numerical dissipation and mixing in simulations of submesoscale and mesoscale baroclinic instabilities over a flat bottom. They found that numerical dissipation can suppress the restratification processes generated by baroclinic instabilities by increasing the background potential energy of the flow. Henell et al. (2023) examined numerical and physical salinity mixing (defined respectively as \mathcal{M}_{num} and \mathcal{M}_{phy} in Section 3) in salinity coordinates with a 1.85 km resolution model of the Baltic Sea. They found that

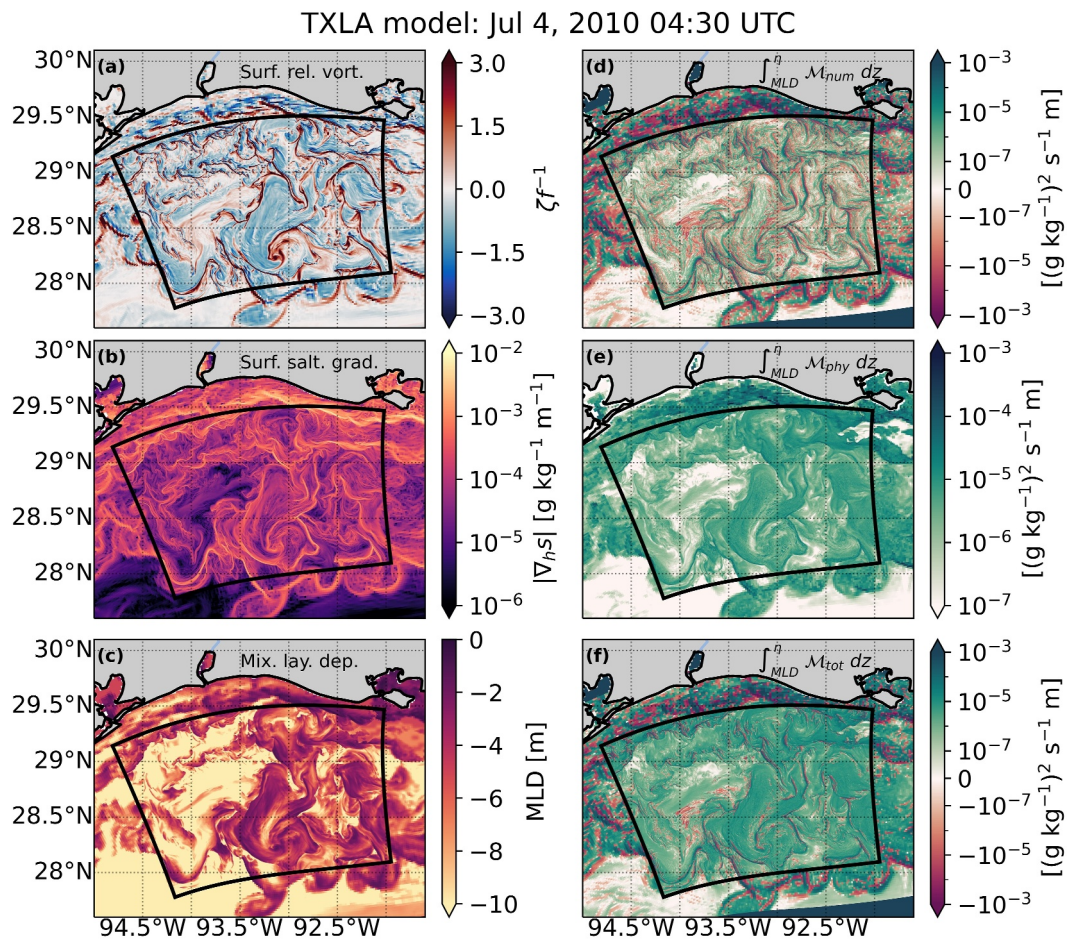


Figure 1. (a) TXLA model surface ζf^{-1} , (b) $|\nabla_h s|$, and (c) mixed layer depth (MLD) on 4 July 2010 04:30 UTC. The child domain is marked by the black box. (d) \mathcal{M}_{num} , (e) \mathcal{M}_{phy} , and (f) \mathcal{M}_{tot} depth-integrated from the base of the mixed layer to the free surface (η). Here, bulk $\mathcal{M}_{num}/\mathcal{M}_{tot} = 24\%$ in the child domain. \mathcal{M}_{num} is elevated near the southern boundary of the parent domain and within several bays/estuaries due to coarse grid resolution and close proximity to the open boundary. The colorbars are saturated to emphasize fronts.

numerical mixing contributed to about half of the integrated dihaline (across-isohaline) exchange flow, with numerical mixing driving the dihaline exchange flow in the opposite direction as physical mixing for many salinity classes.

Schlichting et al. (2023) also quantified volume-integrated numerical and physical salinity mixing in a submesoscale eddy-resolving simulation of the Texas-Louisiana (TXLA) shelf. They found that numerical mixing constitutes about half the total ($\mathcal{M}_{tot} = \mathcal{M}_{num} + \mathcal{M}_{phy}$) mixing and that numerical mixing is correlated with the magnitude of the horizontal salinity gradients $|\nabla_h s| = [(\partial_x s)^2 + (\partial_y s)^2]^{1/2}$, implying that numerical mixing is significant at fronts associated with submesoscale eddies. These eddies are often found during summer as a diurnal land-sea breeze superimposed with the regional inertial period causes freshwater from the Mississippi/Atchafalaya River plume to pool over the shelf (Hetland, 2017), which generates strong inertial currents (DiMarco et al., 2000; Kobashi & Hetland, 2020; Qu, Thomas, Wienkers, et al., 2022). Energetic winds from occasional storms can perturb the eddy field and serve as a rich source of submesoscale variability. An example with the two-way nested TXLA model is shown in Figure 1 to motivate further analysis.

The fronts, marked by normalized relative vorticity $\zeta f^{-1} > 1$, where $\zeta = \partial_x v - \partial_y u$ and f is the Coriolis parameter, are characterized by sharp horizontal salinity gradients. Numerical mixing is depth-integrated from the base of the mixed layer to the free surface and compared with the physical- and total mixing. The mixed layer

depth (MLD) is defined using the standard vertical density difference of 0.03 kg m^{-3} (de Boyer Montégut et al., 2004). As discussed previously, numerical mixing is significant at fronts due to large horizontal salinity gradients. There is also significant negative numerical mixing that corresponds to the anti-diffusive properties of the model's tracer advection scheme.

For the child model domain in Figure 1, numerical mixing constitutes about 24% of the total mixing. Other definitions of MLD may be used (see Thomson & Fine, 2003), but these do not change the general result that the ratio of numerical-to physical mixing grows as the lower limit of integration shoals. For example, depth-integrating over the top 1 m of the water column to the free surface increases this ratio to 52%. When the wind forcing is gentle and the eddies are less perturbed (see Supplemental Movie S1), this ratio can exceed 75%. This implies that even as the horizontal resolution is pushed toward submesoscale resolving, mixing processes in the frontal zone may be numerically driven. More broadly, this reinforces the idea that numerical mixing can dominate in regions where physical mixing is weak (Kalra et al., 2019; Wang et al., 2021).

The primary goal of this paper is to characterize and quantify the numerical mixing in a submesoscale eddy-resolving model, and to gain insight into how this numerical mixing impacts the larger-scale ocean state. It is difficult to address this with a realistic model partly because of the large computational cost, but also because of the variability in model forcing, which changes physical and numerical mixing and thus the larger-scale flow in a nonlinear way. We use an idealized model based on Hetland (2017) that captures many of the characteristics of the submesoscale eddy field seen in the realistic model. We use three different tracer advection schemes following Kalra et al. (2019) in an ensemble of simulations with no explicit horizontal mixing as a way to modify the numerical mixing across different simulations.

We then assess the impact of these advection schemes using alongshore means in the idealized model—an analysis that is not possible in the realistic model. Our primary finding is that numerical mixing suppresses the release of available potential energy, impacting the eddy field and the offshore extent of the fresh water front. Our results support the findings of Mohammadi-Aragh et al. (2015) despite major differences in model configuration. Finally, we examine the utility of adding explicit horizontal mixing as a means of reducing numerical mixing and improving the representation of the ocean state.

2. Numerical Models

The realistic and idealized models are implementations of the Regional Ocean Modeling System (ROMS, Shchepetkin & McWilliams, 2005) configured as part of the Coupled-Ocean-Atmosphere-Waves-Sediment-Transport model (COAWST, ver. 3.7, Warner et al., 2010). ROMS is a hydrostatic, free surface, primitive equation model (Shchepetkin & McWilliams, 2005).

2.1. Realistic ROMS Model

The two-way nested TXLA model setup is described in Schlichting et al. (2023). The sub-domain marked with a black box in Figure 1 is the higher-resolution child model (which is nested in a coarser resolution parent model); in this paper we exclusively use the child model, which uses hourly output frequency. The details necessary to contextualize mixing and compare with the idealized model are provided. The momentum and time-stepping schemes are also listed because they may impact numerical mixing (Ilicak et al., 2012; Lemarié et al., 2015). The model uses a third-order upwind scheme in the horizontal and a fourth-order centered scheme in the vertical for momentum advection (Shchepetkin & McWilliams, 2005). Regarding time-stepping, the barotropic mode is stepped with a third-order Leapfrog-Adams-Moulton scheme with forward-backward feedback. The baroclinic mode is stepped with a third-order Adams Bashforth scheme. Tracers are stepped with a second-order Leapfrog scheme with a trapezoidal corrector. Details of the time-stepping schemes are found in Shchepetkin and McWilliams (2009).

The horizontal resolution of the child model spans from approximately 255 m close to the coast to 357 m near the offshore boundary with a mean resolution of 315 m. The model uses 30 terrain following vertical layers with functions ($Vtransform = 2$, $Vstretching = 4$) and stretching parameters ($\theta_s = 5$, $\theta_b = 0.4$). See Hedström (2009) for further description of the vertical grid parameters. The vertical resolution in the top 1 m of the water column ranges from 13 cm close to the coast to 73 cm near the southern boundary, with a mean resolution of 38 cm. The lowest vertical resolution is about 36 m over the continental slope. As discussed above, this model exhibits

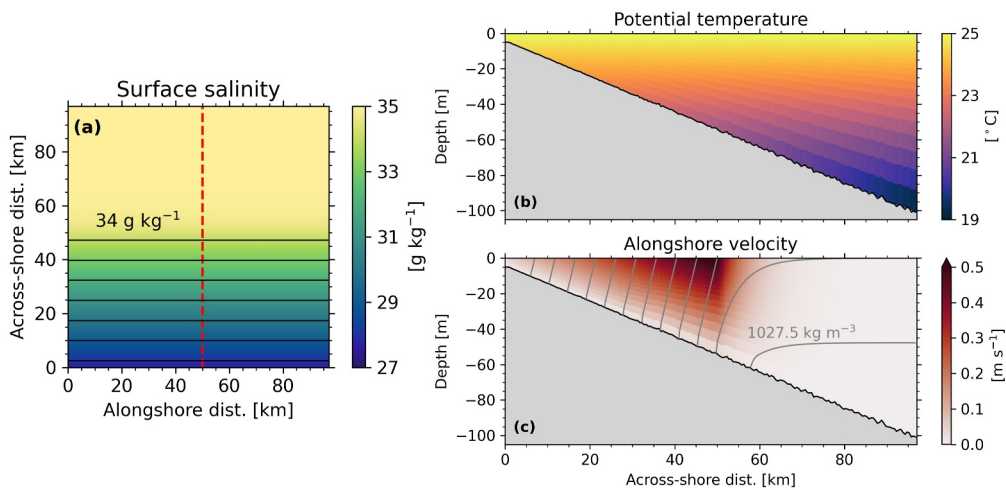


Figure 2. Idealized model initial conditions. (a) Plan view of surface salinity with isohalines overlaid every g kg^{-1} . (b) Cross-sections of potential temperature and (c) alongshore velocity with isopycnals overlaid every 0.5 kg m^{-3} . The cross-sections in panels (b–c) are shown at the red dashed line in panel (a).

significant numerical mixing near the ocean surface. To elucidate the causes and effects of this numerical mixing, we created an idealized model in a similar regime to the realistic model.

2.2. Idealized ROMS Model

The model configuration follows Hetland (2017), but the domain size has been reduced. The initial tracer state is based on a water mass analysis of summer conditions over the TXLA shelf (see his Figure 5). ROMS is configured as a re-entrant shelf with periodic alongshore boundary conditions and a wall at the coast (Figure 2). The domain is 97 km in the along- and across-shore directions with a horizontal resolution of 500 m.

The vertical grid parameters are the same as the realistic model, including the number of vertical layers, transformation functions, and stretching parameters. Hence, the vertical resolution in frontal zones is similar to the realistic model. The minimum water depth is 5 m at the coast and approximately 103 m at the offshore boundary with a bottom slope of 0.001. Over the salinity stratified region, the mean vertical resolution is about 16 cm in the top 1 m of the water column and about 1 m over the entire water column, with the coarsest vertical resolution being 6.8 m close to the bottom. A small amount of random noise equal to 1% of the local depth is added to the bathymetry to force instabilities. The momentum advection scheme and time-stepping scheme are the same as the realistic model. Multidimensional Positive Definite Advection (MPDATA) is used for tracer advection (Smolarkiewicz & Margolin, 1998) for all runs until specified otherwise.

The offshore boundary conditions for the free surface and depth-averaged currents use a Chapman-Flather combination (Chapman, 1985; Flather, 1976). The three-dimensional variables use a no-gradient condition at the offshore boundary. While a no-gradient boundary condition is unrealistic, we analyze all simulations before the eddies interact with the offshore boundary.

The model is run on an f plane with $f = 10^{-4} \text{ s}^{-1}$ ($\sim 43.5^\circ\text{N}$) such that the inertial period is about 17.4 hr. The $k - e$ turbulence closure scheme is used to parameterize vertical mixing (Umlauf & Burchard, 2003; Warner et al., 2005). For the simulations shown in Sections 4.1–4.2, no prescribed horizontal mixing is used. This allows us to directly assess the impacts of numerical mixing on the larger-scale flow for the tracer advection experiments, as done in Mohammadi-Aragh et al. (2015).

The model initial conditions (Figure 2) are specified in terms of two non-dimensional parameters: the Richardson Number ($Ri = N^2 f^2 M^{-4}$) and slope Burger number $S = Nf^{-1}\alpha$. N is the buoyancy frequency, $M^2 = |\nabla_h b|$ is the magnitude of the lateral buoyancy gradients, and α is the bottom slope. The resulting values of Ri and S are 1.0 and 0.1, respectively. The initial salinity varies only in the horizontal with a constant across-shore gradient

inshore of 50 m depth with $M^2 = 10^{-6} \text{ s}^{-2}$. The initial temperature field varies only in the vertical with $N_\theta^2 = 10^{-4} \text{ s}^{-2}$. Density (ρ) uses a linear equation of state:

$$\rho = \rho_0 [1 + \alpha(s - s_0) - \beta(\theta - \theta_0)], \quad (1)$$

where $\rho_0 = 1027 \text{ kg m}^{-3}$ is the reference density, $\alpha = 7.6 \times 10^{-4} (\text{g kg}^{-1})^{-1}$ is the coefficient of haline contraction, s is the absolute salinity, $s_0 = 35 \text{ g kg}^{-1}$ is the reference salinity, $\beta = 1.7 \times 10^{-4} \text{ }^\circ\text{C}^{-1}$ is the coefficient of thermal expansion, θ is the potential temperature, and $\theta_0 = 25^\circ\text{C}$ is the reference potential temperature.

The alongshore flow is initialized with geostrophic vertical shear and no flow at the bottom. The bottom boundary condition uses a logarithmic velocity profile in the bottom boundary layer with the bottom stress defined using a von Kármán constant $\kappa = 0.41$ and bottom roughness $z_0 = 0.003 \text{ m}$.

3. Analysis Methods

3.1. Energetics

Volume-integrated energetics are used to explore how baroclinic instability affects the stratification and eddy kinetic energy. A Reynolds decomposition $\mathbf{u} = \bar{\mathbf{u}} + \mathbf{u}'$ is used to divide the flow into a mean $\bar{\mathbf{u}}$ and fluctuating \mathbf{u}' component, with \mathbf{u} denoting the horizontal velocity vector. Due to the periodic boundary condition, we follow Hetland (2017) and define $\bar{\mathbf{u}}$ with an alongshore mean:

$$\bar{\mathbf{u}} = \frac{1}{L} \int_0^L \mathbf{u} dx \quad (2)$$

such that \mathbf{u}' is the perturbation from the alongshore mean. The local total kinetic energy (KE), mean kinetic energy (MKE), and eddy kinetic energy (EKE) are defined as (Cushman-Roisin & Beckers, 2011):

$$KE = \frac{1}{2}(u^2 + v^2), \quad (3)$$

$$MKE = \frac{1}{2}(\bar{u}^2 + \bar{v}^2), \quad (4)$$

$$EKE = \frac{1}{2}(u'^2 + v'^2). \quad (5)$$

Volume-integrated versions of Equations 3–5 over the salinity stratified region will be used to determine when to analyze mixing and to get an understanding of how wind forcing affects instability development. They are normalized (denoted with n) by the initial MKE (MKE_0) so the initial KE and MKE are one. Thus,

$$KE_n = \frac{\iiint KE dV}{\iiint MKE_0 dV}, \quad (6)$$

$$MKE_n = \frac{\iiint MKE dV}{\iiint MKE_0 dV}, \quad (7)$$

$$EKE_n = \frac{\iiint EKE dV}{\iiint MKE_0 dV}. \quad (8)$$

3.2. Volume-Averaged Salinity Variance

Following Li et al. (2018), we split the salinity into a volume-averaged (\hat{s}) and fluctuating (s') component such that the total variance is written as

$$s'^2 = (s - \tilde{s})^2, \quad \tilde{s} = \frac{1}{V} \iiint s \, dV. \quad (9)$$

This can be decomposed into vertical ($s_v'^2$) and horizontal ($s_h'^2$) components. For example, $s_v'^2 = (s - \tilde{s})^2$ is defined with the vertically averaged salinity \tilde{s} . After some manipulation, it follows that the volume-averaged total salinity variance can be decomposed as:

$$\frac{1}{V} \iiint s'^2 \, dV = \frac{1}{V} \iiint s_h'^2 \, dV + \frac{1}{V} \iiint s_v'^2 \, dV, \quad (10)$$

Which is the volume-averaged version of Equation 8 from Li et al. (2018). $s_h'^2$ is calculated by quantifying s'^2 and $s_v'^2$ individually and subtracting the two such that it is the residual between the volume-averaged total and vertical variance. Previous studies have reported estimates of $\iiint s'^2 \, dV$ (Burchard et al., 2019; Wang & Geyer, 2018). However, this can be difficult to physically interpret because it scales with V . Volume-averaging alleviates this and allows for direct comparison with other estuaries and coastal regions.

3.3. Salinity Mixing

We focus on salinity mixing because the lateral density variations associated with the baroclinic instabilities are dominated by salinity variations. Physical mixing is defined as the dissipation of salinity variance (Burchard & Rennau, 2008; MacCready et al., 2018):

$$\mathcal{M}_{phy} = \underbrace{2\kappa_h(\nabla_h s)^2}_{\mathcal{M}_{phy,h}} + \underbrace{2\kappa_v(\partial_z s)^2}_{\mathcal{M}_{phy,v}}, \quad (11)$$

where κ_h is the horizontal salinity diffusivity and κ_v is the vertical salinity diffusivity. The first term $\mathcal{M}_{phy,h}$ represents the horizontal mixing and $\mathcal{M}_{phy,v}$ represents the vertical mixing. Note that for all experiments in Sections 4.1-4.2, $\mathcal{M}_{phy,h}$ is zero because $\kappa_h = 0$.

Numerical salinity mixing is calculated following Burchard and Rennau (2008):

$$\mathcal{M}_{num} = \frac{A\{s^2\} - (A\{s\})^2}{\Delta t}, \quad (12)$$

where A is the advection operator (i.e., MPDATA) and Δt is the baroclinic timestep. The Burchard and Rennau (2008) algorithm is known to be noisy at the grid-scale, but volume integrals are generally thought to be robust for closed domains (Klingbeil et al., 2014). While the algorithm is improved by Klingbeil et al. (2014), it is not coded into the ROMS source code. As a result, we urge caution when interpreting the amount of negative \mathcal{M}_{num} in Figures 1 and 4.

\mathcal{M}_{num} and $\mathcal{M}_{phy,v}$ are calculated online so errors associated with offline analysis do not contaminate the calculations (Schlichting et al., 2023). For the simulations in Section 4.3 with constant harmonic horizontal mixing, $\mathcal{M}_{phy,h}$ is calculated offline because an analogous online method is not available in the source code. We do not expect errors with offline analysis to be significant in those simulations because κ_h is time-invariant.

3.4. 2D Frontogenesis Function

To better understand the causes of numerical mixing, here we investigate how \mathcal{M}_{num} changes as horizontal tracer gradients are sharpened by frontogenesis and weakened by frontolysis. One way to quantify frontogenesis and frontolysis is to use the frontogenesis function (FGF , Hoskins, 1982; McWilliams, 2021). In two-dimensions, FGF describes whether horizontal advective processes sharpen ($FGF > 0$) or weaken ($FGF < 0$) horizontal buoyancy gradients. FGF is defined as the dot product of the tracer gradients with their Lagrangian rate of change. While typically expressed in terms of horizontal buoyancy gradients, we write FGF in terms of salinity because surface stratification is provided only by salinity:

$$FGF = \frac{1}{2} \frac{D}{Dt} (\nabla_h s)^2, \quad (13)$$

where $\frac{D}{Dt} = \partial_t(\cdot) + \mathbf{u}_h \cdot \nabla_h(\cdot)$ is the material derivative excluding the vertical term.

Barkan et al. (2019) showed that Equation 13 can be normalized in time by f and the local horizontal gradients $(\nabla_h s)^2$, which we define as the normalized frontogenesis function ($nFGF$):

$$nFGF = \frac{1}{2f(\nabla_h s)^2} \frac{D}{Dt} (\nabla_h s)^2. \quad (14)$$

This is useful because the $nFGF$ can be directly compared with other dynamical properties of the flow, such as the normalized divergence $\delta f^{-1} = (\partial_x u + \partial_y v)f^{-1}$. Barkan et al. (2019) showed that divergence is a dominant parameter driving submesoscale frontogenesis, so we expect to see an $\mathcal{O}(1)$ $nFGF$ and δf^{-1} when submesoscale frontogenesis and frontolysis occurs. More broadly, Equation 14 describes the time rate of change of the distance between two isohalines relative to the Coriolis parameter. That is, the normalized rate of cross-frontal convergence and divergence (neglecting non-advection processes). For example, $nFGF = 1$ indicates horizontal salinity gradients will collapse over one rotational timescale. $nFGF = -1$ indicates a front will expand over a rotational timescale.

4. Results

4.1. Impacts of Alongshore Wind Forcing

4.1.1. Overview

Winds are an important driver of submesoscale dynamics over the TXLA shelf. Strong near-inertial motions develop due to near-resonance of the diurnal winds with the regional inertial period (DiMarco et al., 2000). These near-inertial motions can energize fronts, intensify mixing, and facilitate the exchange between surface and bottom waters (Hetland, 2017; Qu, Thomas, Hetland, & Kobashi, 2022; Qu, Thomas, Wienkers, et al., 2022; Schlichting et al., 2023). For example, Figure 9 of Schlichting et al. (2023) demonstrates that volume-integrated \mathcal{M}_{num} and \mathcal{M}_{phy} in the realistic model exhibit order of magnitude variability over an inertial period. While the frontal eddies produced from the idealized model by Hetland (2017) are statistically similar to realistic model, the idealized model lacks near-inertial wind forcing. We seek to make salinity mixing processes in the idealized model more representative of the realistic model by adding near-inertial wind forcing.

First, we ran a simulation for 20 days with no wind forcing (hereafter the unforced case). This is to ensure the energetics are similar to Hetland (2017), who used the same model configuration but in a larger domain. The unforced case also allows us to build an understanding of how salinity mixing processes behave in a configuration with simpler physics. We found this unforced case to have a low ratio (6.5%) of bulk volume-integrated \mathcal{M}_{num} to \mathcal{M}_{phy} . Because of this, we expect that the effects of changes to \mathcal{M}_{num} on the ocean circulation and tracer state would be difficult to identify. To increase this ratio, we performed an ensemble that varied the magnitude of the alongshore near-inertial wind stress amplitude (τ_0^x).

A total of 15 ensemble members were run for 20 days. The members are named according to their value of τ_0^x . The wind stress τ^x is applied uniformly to the ocean surface for each ensemble member as

$$\tau^x = \tau_0^x \sin(0.92ft), \quad (15)$$

where t is time. τ^x is set to zero for the first 3 days of each run to prevent mechanical mixing by the wind from changing the flow before the instabilities start forming on day four (Figures 3a and 3b).

We selected the $\tau_0^x = 0.1$ Pa ensemble member (Figure A1) to be our base case because it had the highest ratio (15.4%) of bulk volume-integrated \mathcal{M}_{num} to \mathcal{M}_{phy} . We expect that this will make it easier to identify the larger-

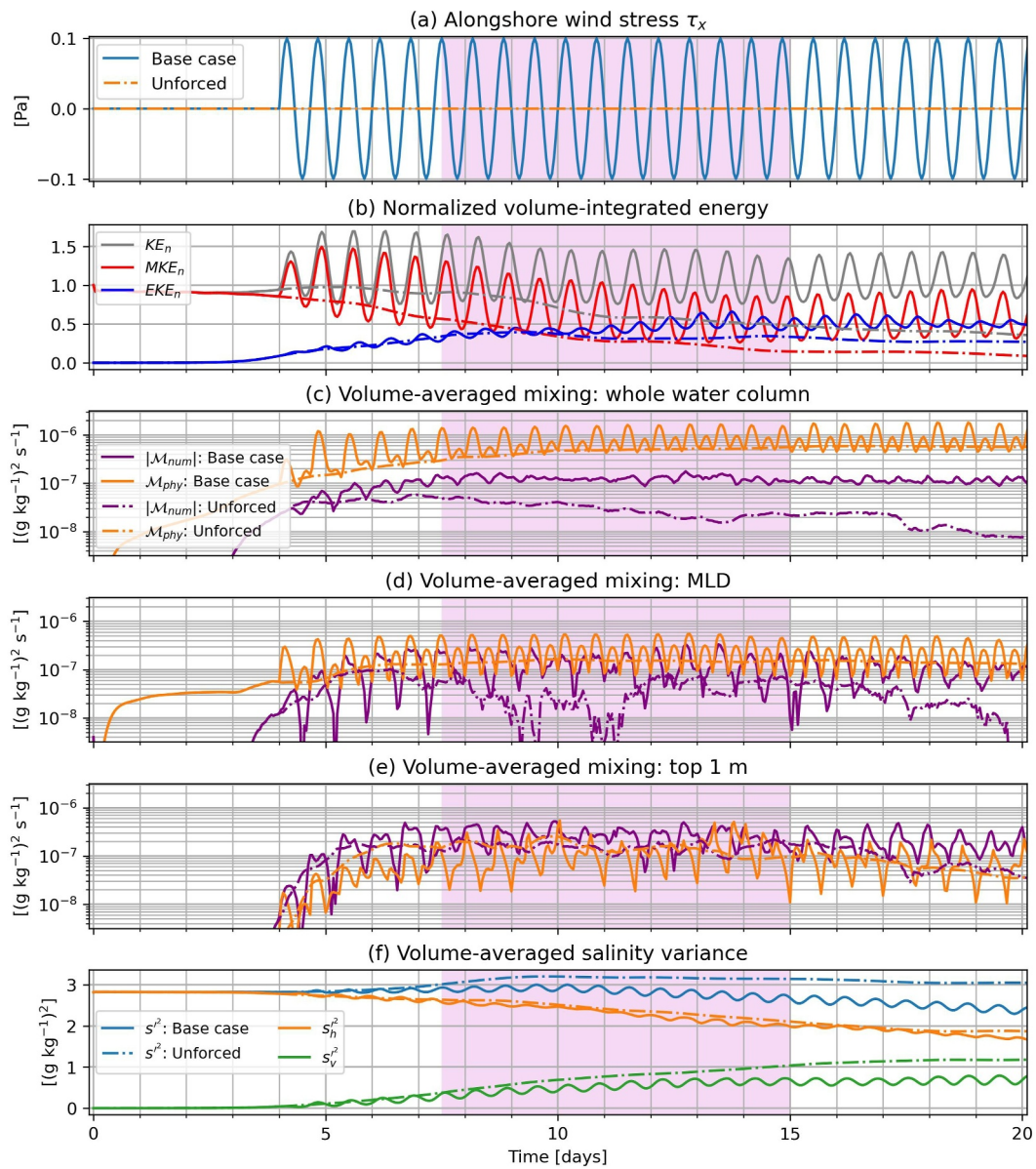


Figure 3. Comparison between the base- and unforced case. Solid lines denote the base case, dash-dotted lines denote the unforced case. (a) Alongshore wind stress τ_x prescribed to each surface grid cell. (b) Normalized, volume-integrated energetics as defined in Section 3.1. (c) Volume-averaged \mathcal{M}_{num} and \mathcal{M}_{phy} for the entire water column. The absolute value is taken to account for negative volume-integrated \mathcal{M}_{num} before the instabilities form. (d–e) As in panel (c), but volume-averaged from the base of the mixed layer to the free surface and from the top 1 m to the free surface. (f) Volume-averaged salinity variance decomposition as defined in Section 3.2. The shaded areas mark the period used for the computation of bulk values.

scale impacts of \mathcal{M}_{num} on the solution for the simulations in Sections 4.2–4.3. The subsubsections below use the metrics outlined in Section 3 to compare between the unforced case and the base case, with a focus on the development of baroclinic instabilities. The amplitude of the near-inertial wind stress in the base case is slightly higher than the diurnal wind stress amplitude in the realistic model. However, we show that the representation of advective frontal processes and \mathcal{M}_{num} (Figure 5) are similar between the base case and realistic model. We provide a synopsis of the near-inertial wind ensemble in Appendix A because the results are not directly related to the objectives of this study. All idealized model quantities hereafter are analyzed inshore of the initial salinity stratified region, which extends to approximately 50 km offshore.

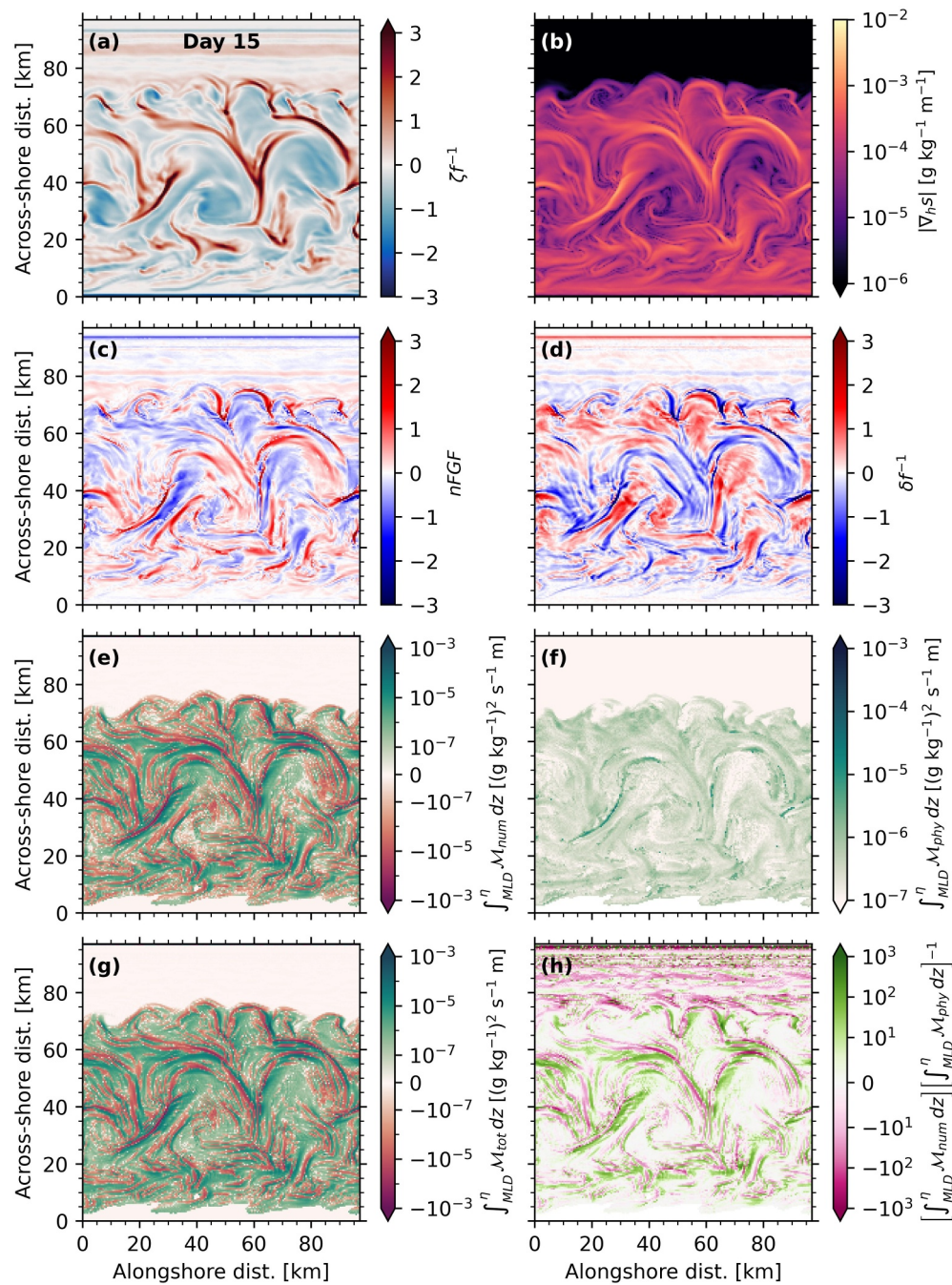


Figure 4. Plan view plots of surface (a) ζf^{-1} , (b) $|\nabla_h s|$, (c) $nFGF$, and (d) δf^{-1} for the base case on day 15 as defined in text. (e) \mathcal{M}_{num} , (f) \mathcal{M}_{phy} , and (g) \mathcal{M}_{tot} depth-integrated from the base of the mixed layer to the free surface. (h) Ratio of depth-integrated \mathcal{M}_{num} over the mixed layer to \mathcal{M}_{phy} . In panel (b), values of $|\nabla_h s|$ offshore of the instabilities are set to $10^{-6} \text{ g kg}^{-1} \text{ m}^{-1}$ because they are poorly defined.

4.1.2. Unforced Case

Normalized volume-integrated energetics for the unforced case are shown by dashed-dotted lines in Figure 3b. As indicated by the EKE_n and consistent with Hetland (2017), the eddy field forms as an organized disturbance after day three. By day 10, the instabilities are mature and never interact with the offshore boundary. The KE_n and MKE_n decrease as the instabilities develop due to bottom friction, which provides a sink of energy via dissipation

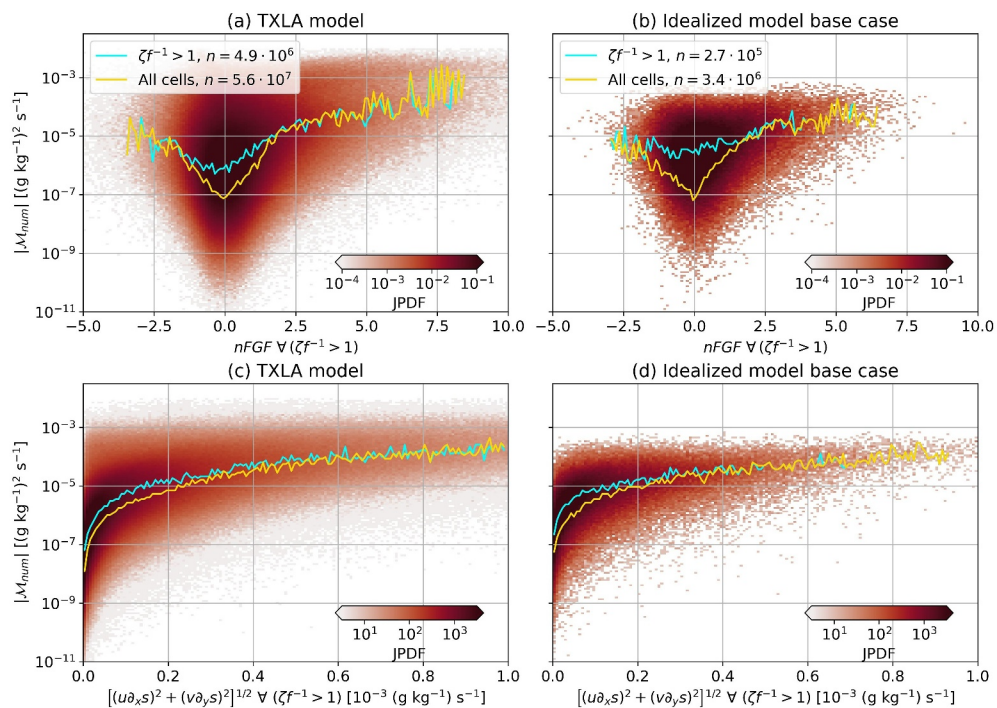


Figure 5. (a) Joint probability density functions (JPDFs) of surface $|\mathcal{M}_{num}|$ and $nFGF$ for the realistic model from 20–26 June 2010 for all fronts ($\zeta/f > 1$). The cyan line highlights the maximum value of the JPDF in each $nFGF$ bin sorted by active fronts and the yellow line marks the same calculation, but for all surface cells. (b) Same as panel (a), but for the base case from days 7.5–15 inshore of the initial salinity stratified region. The total number of cells used to generate each JPDF is shown in the legends. (c–d) Same as panels (a–b), but for the $|\mathcal{M}_{num}|$ and the pointwise salinity transport (Equation 16). In panels (b) and (d), we removed the first three across-shore boundary points near the coastal wall due to strong convergence and divergence regions generated by the winds.

in the bottom boundary layer. As expected, the energetics, mixing quantities, and salinity variance lack the strong near-inertial variability seen in the realistic model (Schlichting et al., 2023).

Volume-averaged \mathcal{M}_{phy} and \mathcal{M}_{num} are shown for three depth ranges: (a) The entire water column (Figure 3c), (b) from the base of the mixed layer to the free surface (Figure 3d), and (c) the top 1 m to the free surface (Figure 3e). All quantities are volume-averaged to enable easy comparison between the different choices of depth range. For all depth ranges, both \mathcal{M}_{phy} and \mathcal{M}_{num} increase as the instabilities form, but they exhibit different temporal variability. For the entire water column, \mathcal{M}_{phy} increases until the instabilities are mature (Figure 3c), then reaches a near steady state. \mathcal{M}_{num} (Figure 3c) maximizes near day seven then decreases for the remainder of the simulation as $|\nabla_h s|$ weakens.

Volume-averaging from the base of the mixed layer (Figure 3d) increases the ratio of bulk \mathcal{M}_{num} to \mathcal{M}_{phy} to 24.9%, indicating that numerical mixing becomes more important in the mixed layer. From days 8–11, \mathcal{M}_{num} declines by over an order of magnitude before returning to previous levels. This variability is not seen in time series of \mathcal{M}_{num} for the base case (Figure 3d) or other ensemble members (not shown). \mathcal{M}_{phy} reaches a near steady state on day 10, as it does when averaged over the entire water column. When volume-averaging from the top 1 m of the water column to the free surface (Figure 3e), \mathcal{M}_{num} rapidly increases as the eddies develop and is comparable to \mathcal{M}_{phy} from days 7.5–15, then gradually declines as the fronts are dissipated by bottom friction. The ratio of bulk \mathcal{M}_{num} to \mathcal{M}_{phy} increases to 104.8%. These results confirm that even in a 500 m resolution idealized model, mixing processes near frontal zones can be driven by \mathcal{M}_{num} .

Energetics and mixing rates are related to the volume-averaged salinity variance (Figure 3f). Until day four, the salinity variance (s'^2) consists only of horizontal variance (s'_h) due to the initial conditions. The vertical variance (s'_v) slightly increases until the instabilities mature on day 10 as the isopycnal slope is reduced. The s'^2 is

gradually converted to $s_v'^2$ via differential advection of horizontal salinity gradients (Li et al., 2018) and restratification by mixed layer instabilities (Boccaletti et al., 2007). In the estuarine community, this process is referred to as tidal straining (Simpson et al., 1990). The key difference in our model is that this process is forced by submesoscale baroclinic instabilities—not tidal forcing. The volume-averaged s'^2 is $\mathcal{O}(3(\text{g kg}^{-1})^2)$, less than half that of the TXLA child model domain (see Figure 7 of Schlichting et al., 2023) and about an order of magnitude less than partially mixed estuaries such as the Hudson or Changjiang (Li et al., 2018; Warner et al., 2020). This is due to the small salinity range used to specify the initial conditions $s = [28, 35]$ (Figure 2a); in contrast, over the TXLA shelf, $s = [0, 37]$. We note that while comparing volume-averaged s'^2 across systems is useful to understand the scale of differences in salinity stratification, the dynamics of our models are fundamentally different from estuarine systems.

4.1.3. Base Case

We show how oscillatory winds change the energetics, salinity mixing processes, and salinity variance components. The solid lines in Figure 3 represent the same quantities discussed above, but for the base case. A time series of the wind stress is shown in Figure 3a. The winds energize the velocity field and add strong near-inertial variability, as shown by the normalized energetics (Figure 3b).

Winds also increase volume-averaged \mathcal{M}_{phy} and \mathcal{M}_{num} for all vertical limits of integration (Figures 3c–3e). The exception is \mathcal{M}_{phy} vertically integrated over the top 1 m (Figure 3e) because the mean vertical salinity gradient is destroyed by the winds (e.g., Figure A1f). The oscillations shown in the volume-averaged mixing quantities (Figures 3c–3e) are qualitatively related to deepening of the mixed layer (not shown). The ratio of bulk \mathcal{M}_{num} to \mathcal{M}_{phy} calculated for the whole water column is 15.4%, for the mixed layer is 49.3%, and for the top 1 m of the water column is 210.8%.

The salinity variance (s'^2) and its vertical component $(s_v'^2)$ are lower in the base case than in the unforced case (Figure 3f) because the base case has higher \mathcal{M}_{phy} (Figure 3c), which destroys vertical salinity variance by definition. The horizontal component of the salinity variance $(s_h'^2)$ is similar between the two cases despite the increase in \mathcal{M}_{num} . This is partially because both cases lack explicit horizontal mixing and \mathcal{M}_{num} is still small relative to \mathcal{M}_{phy} . In addition, the base case has sharper fronts than the unforced case (as approximated by $|\nabla_h s|$, Figure A1e), which can compensate for the destruction of $s_h'^2$ by \mathcal{M}_{num} .

To qualitatively demonstrate that the base case eddies in the idealized model are similar to the realistic model, Figures 4a–4d shows plan view plots of ζf^{-1} , $|\nabla_h s|$, δf^{-1} , and $nFGF$ on day 15 at the surface, respectively. An animation of Figure 4 is shown in Supplemental Movie S2 so it can be directly compared with the realistic model (Supplemental Movie S1). As Barkan et al. (2019) found, $nFGF$ is negatively correlated with δf^{-1} . That is, frontogenesis is associated with convergent flows and frontolysis is associated with divergent flows.

The depth-integrated \mathcal{M}_{num} , \mathcal{M}_{num} , \mathcal{M}_{tot} , and ratio of \mathcal{M}_{num} to \mathcal{M}_{phy} over the mixed layer are shown in Figures 4e–4h. As with the realistic model, \mathcal{M}_{num} can exceed \mathcal{M}_{phy} by several orders of magnitude at the fronts and is associated with sharp $|\nabla_h s|$. There is substantial negative \mathcal{M}_{num} (Figure 4e) that is noisy at the grid scale, which we suspect is a byproduct of the Burchard and Rennau (2008) algorithm. The \mathcal{M}_{phy} is generally weaker in the idealized model because there are no surface and lateral boundary buoyancy fluxes, which provide additional sources of salinity variance that can be destroyed by mixing.

A statistical comparison between the realistic model and base case is shown with joint probability density functions (JPDFs) of $|\mathcal{M}_{num}|$ and $nFGF$ in the top vertical layer (i.e., the surface) for cells with submesoscale fronts ($\zeta f^{-1} > 1$) in Figure 5. The absolute value of \mathcal{M}_{num} is used to account for the negative values. The cyan line marks the maximum probability of $|\mathcal{M}_{num}|$ in each $nFGF$ bin sorted by submesoscale fronts ($\zeta f^{-1} > 1$). The yellow line displays the same quantity as the cyan line, but for the JPDF (not shown) that uses all cells in the top vertical layer. The TXLA model JPDF (Figure 5a) was constructed using a week of model output when the wind forcing is gentle and the eddies are more representative of summer conditions (see Supplemental Movie S1).

Several conclusions are drawn from Figures 5a and 5b: (a) the strongest occurrences of frontogenesis produce the sharpest horizontal salinity gradients and thus the strongest $|\mathcal{M}_{num}|$, (b) the distribution of $|\mathcal{M}_{num}|$ experiences the largest variability when frontogenesis and frontolysis are weak (i.e., $nFGF \sim [-1, 1]$), which constitutes the majority of grid cells at the ocean surface, (c) frontogenesis and frontolysis in the base case (Figure 5b) are representative of the realistic model (Figure 5a), and (d) $nFGF$ is skewed toward frontogenesis. An interesting result is that $|\mathcal{M}_{num}|$ is significant even for strongly frontolytic processes. These results reinforce the idea that horizontal tracer gradients are a dominant parameter modulating \mathcal{M}_{num} , even if those gradients are being instantaneously weakened.

The base case features a smaller range of $|\mathcal{M}_{num}|$ and $nFGF$ due to the coarser horizontal resolution and a smaller salinity range (see Section 2). The impacts of horizontal resolution on \mathcal{M}_{num} are further elucidated by the cyan lines, where areas with weak frontogenesis and frontolysis feature $|\mathcal{M}_{num}|$ maxima (Figure 5b) about half an order of magnitude stronger than the same range for the realistic model (Figure 5a). We would expect these differences to decrease if the horizontal resolution of the base case was closer to the realistic model. In addition, the maximum $|\mathcal{M}_{num}|$ in each $nFGF$ bin for the entire ocean surface are similar when $|nFGF| \sim 2$. While determining a proper scaling between ζf^{-1} and $nFGF$ or δf^{-1} is beyond the scope of this paper, it is intuitive that the strongest fronts and eddies correspond to regions of strong frontogenesis and frontolysis.

To complement our analysis of the $nFGF$, we also present JPDFs of $|\mathcal{M}_{num}|$ and the pointwise horizontal salinity transport (T_{salt}) for all cells with submesoscale fronts in the top vertical layer for both models (Figures 5c and 5d). T_{salt} is defined as the magnitude of the horizontal salinity advection:

$$T_{salt} = [(u\partial_x s)^2 + (v\partial_y s)^2]^{1/2}. \quad (16)$$

JPDFs of T_{salt} and $|\mathcal{M}_{num}|$ are informative because $|\mathcal{M}_{num}|$ is expected to be larger in places where large amounts of salt are advected between grid cells. The cyan and yellow lines represent the same quantities as in Figures 5a and 5b, but use the maximum JPDF value in each T_{salt} bin.

Figures 5c and 5d demonstrate that increasing T_{salt} increases $|\mathcal{M}_{num}|$. That is, stronger horizontal tracer advection is associated with larger discretization errors and thus stronger $|\mathcal{M}_{num}|$. These results offer a possible explanation for why $|\mathcal{M}_{num}|$ remains large even for fronts undergoing frontolysis. The divergent processes driving frontolysis may be associated with a large horizontal advective salinity flux, which in turn elevates $|\mathcal{M}_{num}|$, but further analysis is needed to confirm this. The maxima lines are in agreement with the trends in Figures 5a and 5b. That is, fronts exhibit higher $|\mathcal{M}_{num}|$ compared to non-frontal cells at the ocean surface, even those fronts that are associated with small advective salinity fluxes. Figures 5c and 5d provides further evidence that the base case produces an ocean state with similar physical and numerical process representation as compared to the realistic model.

To summarize, oscillatory near-inertial winds offer the advantage of making the idealized model more realistic by resonantly forcing near-inertial motions. The wind stress amplitude used for the base case (0.1 Pa) increases the amount of \mathcal{M}_{num} and \mathcal{M}_{phy} relative to the unforced case, but particularly increases \mathcal{M}_{num} in the mixed layer. The base case produces an ocean state with stronger frontogenesis, frontolysis, and pointwise salinity transport, resulting in a simulation with more \mathcal{M}_{num} .

4.2. Impacts of Tracer Advection Schemes

4.2.1. Overview

We study the sensitivity of the base case with several commonly used tracer advection schemes available in the COAWST source code. We do not perform a detailed evaluation of these schemes numerical performance, which has been done more thoroughly in other studies detailed below. Rather, we aim to gain a general understanding of the range of impacts on the larger-scale ocean circulation when using different high-order schemes.

For two sets of experiments, no distinction is made for the horizontal and vertical advection schemes. They are MPDATA (Smolarkiewicz, 1984; Smolarkiewicz & Margolin, 1998; Waruszewski et al., 2018) and third high-order spatial interpolation at the middle temporal level with a total variation diminishing scheme (HSIMT, Sweby, 1984; Wu, 2023; Wu & Zhu, 2010). MPDATA is second-order accurate and HSIMT is third-order

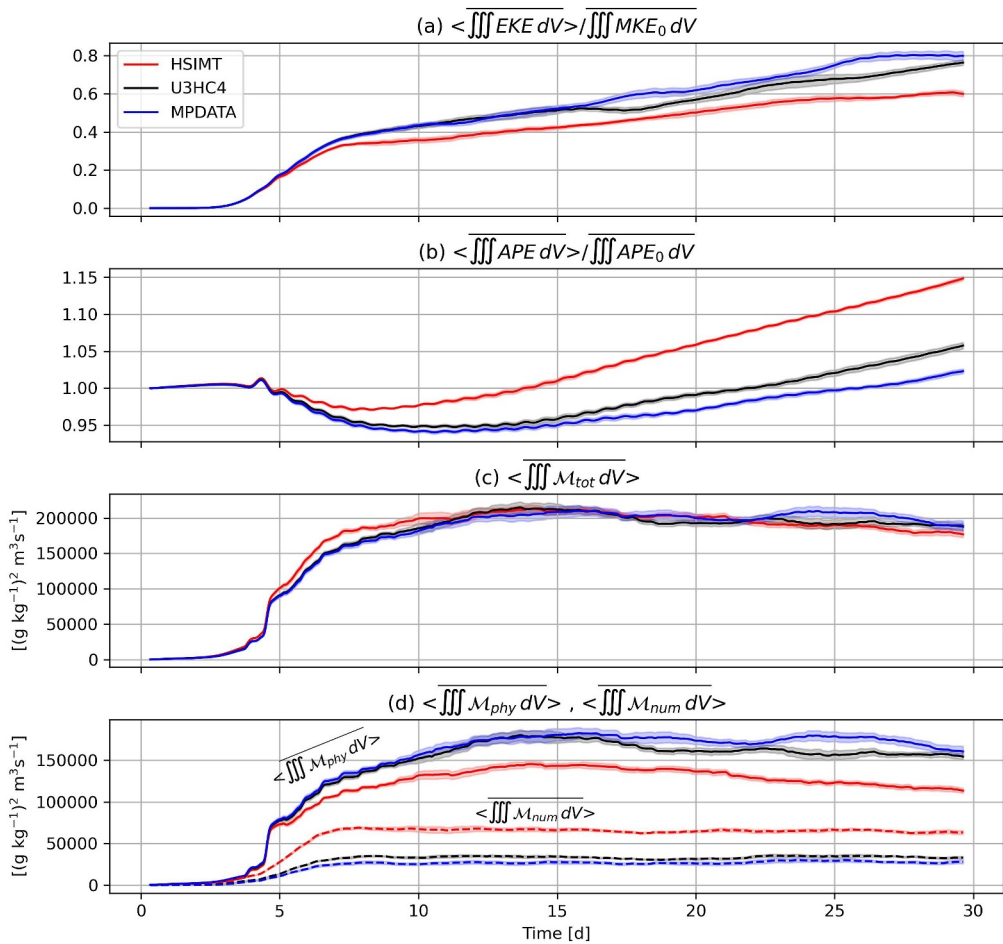


Figure 6. (a) Time series of $EKE_{n,ens}$, (b) $APE_{n,ens}$, (c) $M_{tot,ens}$, and (d) $M_{phy,ens}$ and $M_{num,ens}$ as defined in text. The angle brackets denote a 16 hr rolling mean and the overline denotes an ensemble average. The shaded areas represent values within the 95% confidence intervals. In panel (d), $M_{phy,ens}$ is shown with solid lines and $M_{num,ens}$ is shown with dashed lines.

accurate. The third set of experiments pairs a third-order upwind scheme for horizontal advection with a fourth-order centered scheme for vertical advection (U3HC4, Shchepetkin & McWilliams, 1998; Shchepetkin & McWilliams, 2005). The details of each scheme can be found in the references above and are summarized in Section 2.2 of (Kalra et al., 2019).

To ensure that differences between advection schemes are not due to a specific set of initial conditions, we perform an ensemble of the base case by varying only the model bathymetry. To do so, the 1% random noise added to the bathymetry is regenerated for each ensemble member. This will slightly change how the instabilities form. Each ensemble member is run for 30 days in a larger across-shore domain (194 km) so the eddies never interact with boundary.

Eight ensemble members per advection scheme were sufficient to capture variability caused by changing the bathymetry noise. This is shown in Figure 6 with the 95% confidence intervals of volume-integrated ensemble-averaged energetics and mixing quantities. All quantities are smoothed with a 16 hr rolling mean (denoted with angle brackets) to remove the variability caused by the wind and improve readability. Volume integration was performed from the coast to 97 km across-shore, which represents the boundary of the original domain. This is because the eddies from several ensemble members approximately reach this location by day 30 (not shown).

4.2.2. Energetics, Mixing, and the Tracer Fields

We start with analysis of the double-averaged, volume-integrated *EKE*:

$$EKE_{n,ens} = \langle \overline{\iiint EKE \, dV} \rangle \left[\overline{\iiint MKE_0 \, dV} \right]^{-1}. \quad (17)$$

Differences between schemes are detectable shortly after the eddies begin forming. The HSIMT simulations feature the lowest $EKE_{n,ens}$ over the 30 days, with 25% less $EKE_{n,ens}$ than the other schemes by day 30. The confidence intervals of $EKE_{n,ens}$ between the U3HC4 and MPDATA simulations overlap for most of the 30 days, requiring further analysis to identify whether the representation of the ocean state is different between schemes.

We also compare the tracer advection schemes using the available potential energy (*APE*). Hetland (2017) defines this locally as

$$APE = -\rho_0 b' z, \quad (18)$$

where $b' = b - b_{ref}$ is the buoyancy anomaly with reference buoyancy b_{ref} . Here, $b = -g(\rho_0 - \rho)\rho_0^{-1}$. b_{ref} is defined using the temperature-dependent part of Equation 1 so the across-shore buoyancy gradient is zero. Formally, *APE* should also include contributions from the sea surface height anomalies, but these were determined to be negligible (not shown, see Appendix B of Hetland, 2017).

The *APE* is related to the isopycnal slope (Brink, 2016; Brink & Seo, 2016). As baroclinic instabilities relax the mean flow, the slope of the initially tilted isopycnals is reduced (Hetland, 2017; Zhang & Hetland, 2018). A simulation with more developed eddies (higher *EKE*) will feature less *APE* and flatter isopycnals because the eddies have extracted *APE* from the horizontal density gradient. On the other hand, a simulation with less developed eddies (lower *EKE*) will feature more *APE* and steeper isopycnals. We return to this point later.

The volume-integrated double-averaged *APE* is normalized by its initial value APE_0 :

$$APE_{n,ens} = \langle \overline{\iiint APE \, dV} \rangle \left[\overline{\iiint APE_0 \, dV} \right]^{-1}. \quad (19)$$

The $APE_{n,ens}$ is shown in Figure 6b for each scheme and is consistent with arguments posed above. By day five, the HSIMT simulations have more $APE_{n,ens}$ than the other schemes and this grows with respect to time. The U3HC4 simulations have more $APE_{n,ens}$ than the MPDATA simulations over the 30 days, although these differences remain negligible until day 15. The $APE_{n,ens}$ for all schemes decreases below their initial values, plateaus, then eventually rise above their initial values. The $APE_{n,ens}$ decreases as the isopycnal slope is reduced in the initially stratified region. Later increases in the $APE_{n,ens}$ are caused by wind-induced mixing offshore of the eddy field where the isopycnal slope is controlled by temperature. There, wind mixing increases the isopycnal slope, which compensates for the $APE_{n,ens}$ decrease in the initially stratified region. If volume-integration were performed inshore of the initial salinity stratified region, $APE_{n,ens}$ would continuously decline below its initial values (not shown).

To examine possible causes for the differences in energetics across advection schemes, Figures 6c–6e displays time series of the volume-integrated, double-averaged mixing quantities. For example, the total mixing is now defined as:

$$\mathcal{M}_{tot,ens} = \langle \overline{\iiint \mathcal{M}_{tot} \, dV} \rangle. \quad (20)$$

Similar equations are obtained for the physical mixing ($\mathcal{M}_{phy,ens}$) and numerical mixing ($\mathcal{M}_{num,ens}$). Bulk values and ratios of these quantities are shown in Table 1 to supplement Figure 6. The HSIMT simulations have substantially more numerical mixing than the other schemes and moderately less physical mixing. The $\mathcal{M}_{phy,ens}$ constitutes 86% of $\mathcal{M}_{tot,ens}$ for the MPDATA simulations, 83% for U3HC4, and 66% for HSIMT. The $\mathcal{M}_{tot,ens}$ is similar across all advection schemes. $\mathcal{M}_{num,ens}$ is larger in the HSIMT simulations at all times relative to the other schemes. These results suggest that as instabilities form, the increased $\mathcal{M}_{num,ens}$ suppresses instability growth by

Table 1

Sensitivity of Ensemble-Averaged Mixing Quantities to the Tracer Advection Scheme

Scheme	$\Sigma M_{phy,ens}$	$\Sigma M_{num,ens}$	$\Sigma M_{tot,ens}$	$M_{phy,ens}/M_{tot,ens}$	$M_{num,ens}/M_{tot,ens}$
MPDATA	9.90	1.59	11.49	0.86	0.14
U3HC4	9.39	1.98	11.37	0.83	0.17
HSIMT	7.66	3.88	11.54	0.66	0.34

Note. Ratios of bulk (denoted by Σ) volume-integrated physical, numerical, and total mixing inshore of 97 km. Bulk values have units of $10^7 (\text{g kg}^{-1})^2 \text{ m}^3 \text{ s}^{-1}$.

preventing the release of $APE_{n,ens}$. Weaker instabilities are associated with lower $M_{phy,ens}$ because the isopycnals are more vertical, which causes $\partial_z s$ to be smaller.

Finally, we show how differences in energetics observed across advection schemes manifest in the tracer fields. Figure 7 shows the differences in salinity and density structure across advection schemes. Cross-sections of alongshore- and ensemble-averaged salinity (\bar{s}) are plotted on day 7.5 and on day 30 for MPDATA (Figures 7a and 7b) and the salinity difference $\Delta\bar{s}$ from the MPDATA simulation is plotted for other schemes (Figures 7c–7f). Positive values of $\Delta\bar{s}$ means the scheme is saltier than MPDATA, whereas negative values indicate it is fresher. Alongshore- and ensemble-averaged isopycnals are also overlaid every 0.5 kg m^{-3} . The $1,027 \text{ kg m}^{-3}$ isopycnal approximately represents the boundaries of the salinity stratified region.

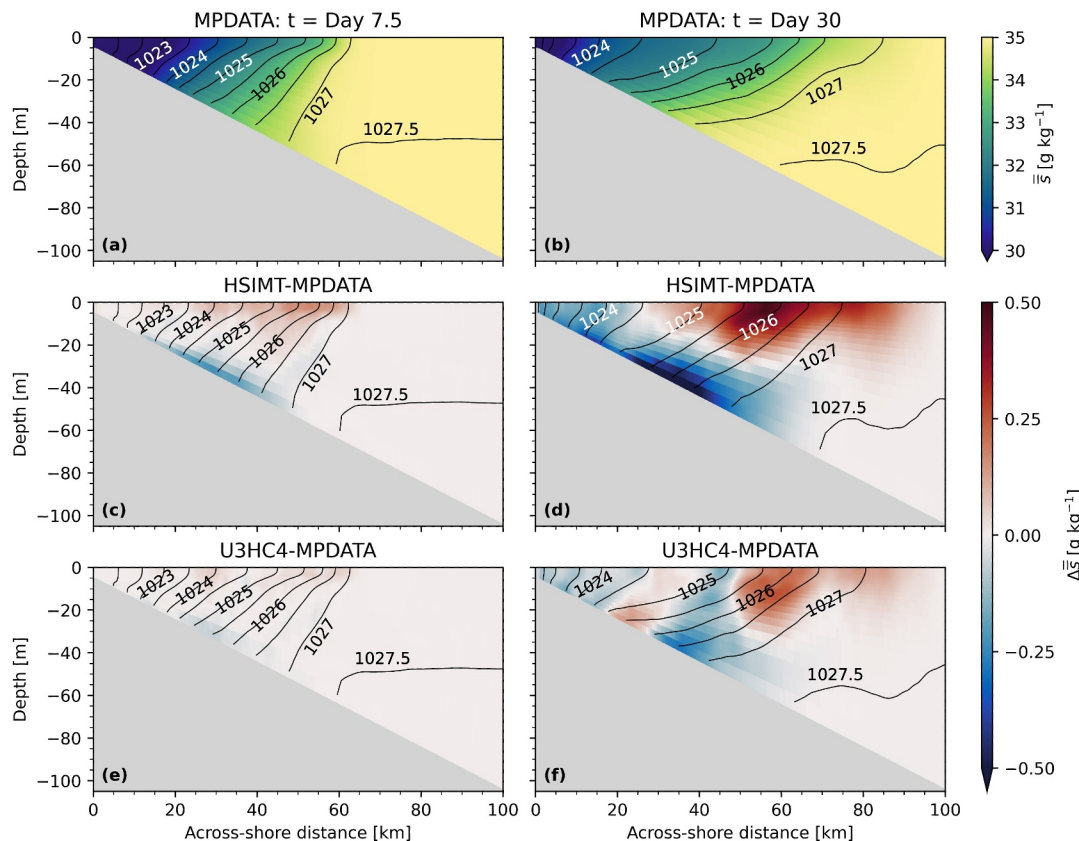


Figure 7. Cross-sections of alongshore- and ensemble-averaged salinity (indicated by double overline) for the MPDATA simulations on panel (a) day 7.5 and (b) day 30. Relative differences between the same quantities for the (c–d) HSIMT and (e–f) U3HC4 simulations. Isopycnals are overlaid every 0.5 kg m^{-3} for each scheme. Note the bathymetry noise is smoothed by the averaging, so the isopycnals do not appear to reach the seafloor.

On day 7.5, the $\Delta\bar{s}$ between the HSIMT and MPDATA simulations is small, with a two layer structure that is fresher near the bottom and saltier from the middle of the water column to the surface (Figure 7c). The differences between the U3HC4 and MPDATA simulations are also small, and the $\Delta\bar{s}$ is slightly fresher toward the bottom inshore of the initially stratified region and saltier near the surface (Figure 7e). By day 30, the mean isopycnal slope has reduced for all advection schemes. The surface position of the $1,027 \text{ kg m}^{-3}$ isopycnal is approximately 10 km further offshore in the MPDATA simulations than the HSIMT simulations (Figure 7d) and five km further offshore than in the U3HC4 simulations (Figure 7f). Likewise, the $\Delta\bar{s}$ between HSIMT and MPDATA is saltier by up 0.5 g kg^{-1} .

These results suggest the impacts of numerical mixing in our model are similar to larger-scale models and *not* like implicit LES models (see Section 1), where numerical dissipation is used as a substitute for subgrid-scale mixing parameterizations (Danilov et al., 2017). In other words, the ocean circulation and tracer state are sensitive to the type of mixing that occurs in simulations of submesoscales with primitive equation ocean models, even if the total mixing is similar across different advection schemes. These results are generally consistent with the findings of Mohammadi-Aragh et al. (2015), who found that advection schemes with larger numerical mixing delayed restratification processes due to baroclinic instability.

4.3. Impacts of Explicit Horizontal Mixing

4.3.1. Experiment Design

Previous studies (Ilicak et al., 2012; Megann & Storkey, 2021) have shown that explicit horizontal mixing can reduce the amount of numerical mixing in a simulation. We hypothesize that small amounts of horizontal mixing will increase the *EKE* and reduce the *APE* across all advection schemes by reducing numerical mixing at the fronts, thereby improving the representation of submesoscale processes. We expect numerical mixing to behave differently than physical mixing in frontal zones. This is because numerical mixing depends on flow velocities in addition to tracer gradients and has a strong negative component (see Supplemental Movies S1–S2) that is spatially and temporally heterogeneous. On the other hand, physical mixing is positive definite and depends only on the magnitude of tracer gradients when a constant diffusivity is used.

We performed two sets of experiments with different horizontal mixing parameterizations (Figure 8). All simulations use the same bathymetry and rotate the mixing tensors along geopotential surfaces. Note that geopotential-aligned mixing tensors are commonly used in shallow domain regional models that resolve eddy driven mixing (see Section 3.4 of Marchesiello et al., 2009). All aspects of the model configuration and analysis are the same as in Section 4.2 except for the amount of prescribed horizontal mixing. The first set of experiments ($n = 24$, 8 for each advection scheme) vary the magnitude of constant horizontal viscosity (ν_h) and diffusivity (κ_h) coefficients combined with a harmonic operator. The values of ν_h range from $0.5 \text{ m}^2 \text{ s}^{-1}$ to $100.0 \text{ m}^2 \text{ s}^{-1}$ with corresponding $\kappa_h = \nu_h/5$. Our choice for the ratio of κ_h to ν_h is the same as the realistic model.

The horizontal grid Reynolds number Re_Δ characterizes the ratio of the horizontal inertial forces at the grid-scale to the horizontal viscous forces at the grid-scale:

$$Re_\Delta = \frac{U\Delta X}{\nu_h} \quad (21)$$

where U is a characteristic velocity scale and ΔX is the horizontal resolution. Previous studies (Ilicak, 2016; Ilicak et al., 2012; Megann & Storkey, 2021) have shown that simulations with large Re_Δ may become saturated with numerical mixing and thus compromise the representation of the ocean state. U is defined here as the maximum magnitude of the initial alongshore velocity in thermal wind balance ($U \sim 0.52 \text{ m s}^{-1}$). This results in Re_Δ ranging from 2.6 to 520 across all simulations, as shown on the bottom of Figures 8g and 8h.

The second experiment set ($n = 3$) uses the Smagorinsky scheme (Smagorinsky, 1963) to compute time- and deformation-dependent viscosity and diffusion coefficients. Both coefficients are paired with a biharmonic operator. Re_Δ values are not calculated for these experiments because ν_h is time-dependent. Likewise, we do not calculate $M_{phy,h}$ because an online option is not available and the time dependency of κ_h could introduce substantial errors into the calculations (Schlichting et al., 2023).

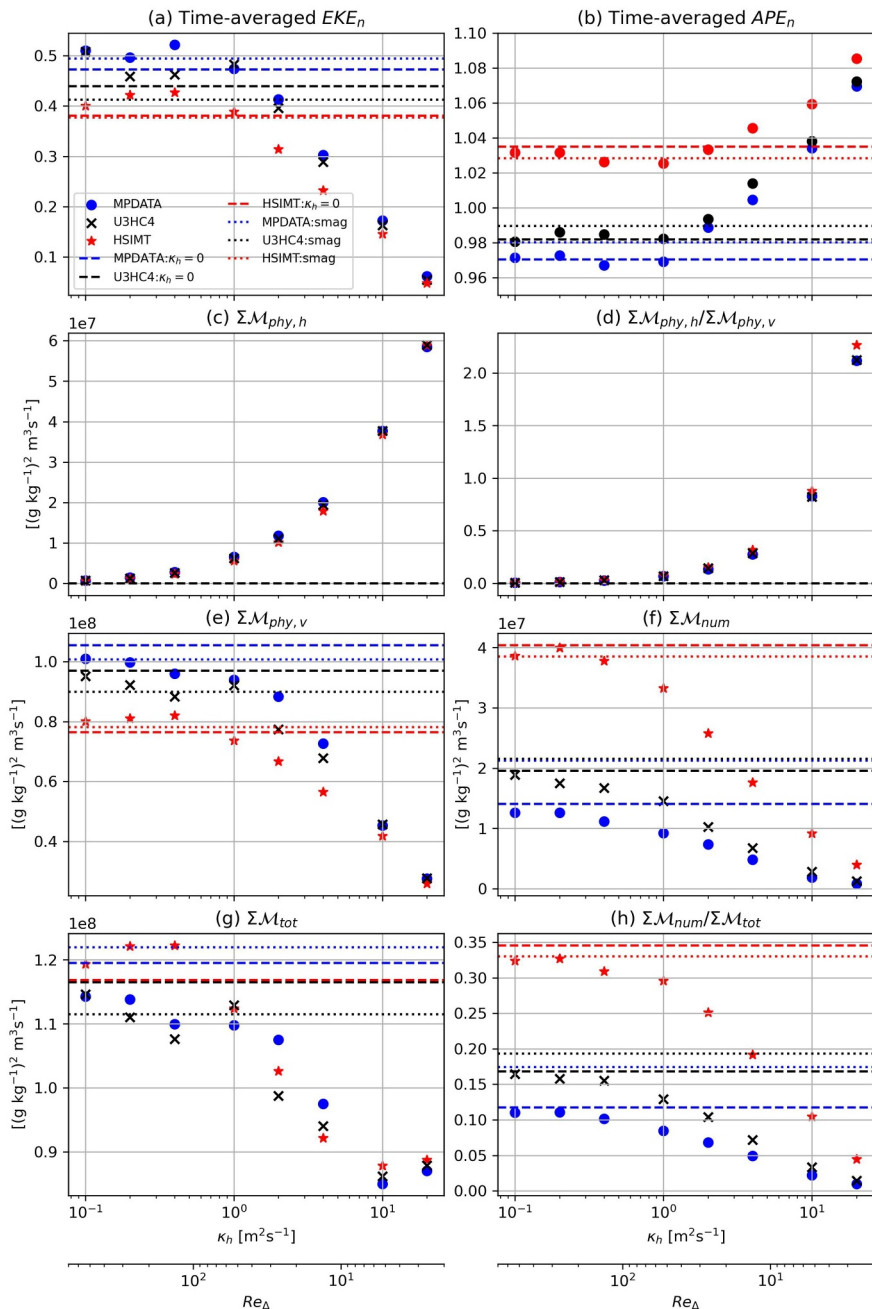


Figure 8. Horizontal mixing experiments, with each symbol or line representing a different numerical simulation. All quantities are analyzed over 30 days and up to 97 km offshore. (a) Time-averaged EKE_n and (b) APE_n . (c) Bulk $M_{phy,h}$. (d) Ratio of bulk $M_{phy,h}$ to $M_{phy,v}$. (e) Bulk $M_{phy,v}$, (f) M_{num} , and (g) M_{tot} . (h) Ratio of bulk M_{num} to M_{tot} . The MPDATA simulations are marked by blue colors, U3HC4 by black colors, and HSIMT by red colors. Dashed lines mark the simulations with no explicit horizontal mixing, dotted lines are for the Smagorinsky simulations. The x-axes display κ_h for the constant, harmonic experiments. Re_{Δ} is shown below the x-axes of panels (g–h). Note the Smagorinsky simulations are not shown in panels (c–d) because calculations are unavailable.

4.3.2. Energetics

Figure 8a shows the time-averaged (over the 30 days), volume-integrated, EKE_n (Equation 8) as a function of κ_h and Re_{Δ} . The time-averaged, volume-integrated APE normalized by its initial value APE_n (same as Equation 19 without the ensemble or rolling averages) is shown in Figure 8b. Blue colors show the MPDATA simulations,

black colors show the U3HC4 simulations, and red colors show the HSIMT simulations. Simulations with no horizontal mixing are shown by dashed lines, and the Smagorinsky simulations are shown with dotted lines.

Beginning with the constant mixing coefficient experiments, the parameter space can be divided into two regimes. When $\kappa_h < 1.0 \text{ m}^2 \text{ s}^{-1}$ ($Re_\Delta > 52$), the time-averaged EKE_n is higher for all advection schemes than the simulations without explicit horizontal mixing (Figure 8a). When $\kappa_h > 1.0 \text{ m}^2 \text{ s}^{-1}$ ($Re_\Delta < 52$), the time-averaged EKE_n rapidly decreases relative to the simulations without any explicit horizontal mixing for all advection schemes. For the experiments with larger mixing coefficients (e.g., the $\kappa_h = 20 \text{ m}^2 \text{ s}^{-1}$, $Re_\Delta = 2.6$ case) a submesoscale eddy field does not develop, which is implied but not qualitatively shown. For all mixing coefficients, the HSIMT simulations have less time-averaged EKE_n compared to the other schemes. The MPDATA simulations have slightly more time-averaged EKE_n compared to the U3HC4 simulations for half the simulations.

The time-averaged APE_n plots (Figure 8b) display the same regimes as the time-averaged EKE_n . When $\kappa_h < 1.0 \text{ m}^2 \text{ s}^{-1}$, the time-averaged APE_n remains similar to the simulations with no horizontal mixing for MPDATA and U3HC4 and slightly decreases in the HSIMT simulations. Several of the MPDATA and U3HC4 simulations have slightly more time-averaged APE_n despite higher time-averaged EKE_n , which is because the explicit horizontal mixing also impacts the shear instabilities that form seaward of the salinity stratified region. When $\kappa_h > 1.0 \text{ m}^2 \text{ s}^{-1}$, the time-averaged APE_n increases as wind mixing destroys the temperature-based vertical stratification seaward of the salinity stratified region. For all mixing coefficients, the HSIMT simulations have more time-averaged APE_n compared to other schemes and the U3HC4 simulations have slightly more time-averaged APE_n than the MPDATA simulations.

The Smagorinsky simulations are more difficult to interpret, with the results being scheme dependent. The MPDATA simulation has slightly more time-averaged EKE_n and APE_n relative to the simulation without explicit horizontal mixing (Figures 8a and 8b). The U3HC4 simulation has slightly less time-averaged EKE_n but more APE_n relative to the simulation without explicit horizontal mixing. In the HSIMT simulation, there is nearly no difference in the time-averaged EKE_n relative to the case without explicit horizontal mixing, but the APE_n slightly decreases.

4.3.3. Mixing

The bulk, volume-integrated explicit horizontal salinity mixing $\mathcal{M}_{phy,h}$ and other mixing quantities are shown in Figures 8c–8h. For the constant coefficient experiments, the bulk $\mathcal{M}_{phy,h}$ (Figure 8c) and ratio of bulk $\mathcal{M}_{phy,h}$ to $\mathcal{M}_{phy,v}$ increase (Figure 8d) as the mixing coefficients increase. When $\kappa_h < 1 \text{ m}^2 \text{ s}^{-1}$ (the first regime), the ratio of bulk $\mathcal{M}_{phy,h}$ to $\mathcal{M}_{phy,v}$ ranges from less than 1%–7% and rapidly increases for the second regime. The bulk $\mathcal{M}_{phy,v}$ (Figure 8e), \mathcal{M}_{num} (Figure 8f), and \mathcal{M}_{tot} (Figure 8g) decrease for all MPDATA and U3HC4 simulations relative to the simulations without explicit horizontal mixing. The HSIMT simulations follow the same trends for \mathcal{M}_{num} , however, there is a slight increase in the $\mathcal{M}_{phy,v}$ and therefore the \mathcal{M}_{tot} when $\kappa_h \leq 0.4 \text{ m}^2 \text{ s}^{-1}$.

For all experiments, the HSIMT simulations have more \mathcal{M}_{num} compared to the other schemes and less $\mathcal{M}_{phy,v}$. As with the experiments in Section 4.2, the U3HC4 simulations have more \mathcal{M}_{num} and less $\mathcal{M}_{phy,v}$ than the MPDATA simulations. The ratio of bulk \mathcal{M}_{num} to \mathcal{M}_{tot} (Figure 8h) decreases for all experiments across all advection schemes relative to the simulations without explicit horizontal mixing. The HSIMT simulations have the highest ratio of \mathcal{M}_{num} to \mathcal{M}_{tot} for all simulations, followed by U3HC4 with the second highest, and MPDATA with the lowest.

For the Smagorinsky simulations, the bulk mixing quantities are also scheme dependent relative to the simulations without explicit horizontal mixing. For the MPDATA and U3HC4 simulations, there is a slight decrease in bulk $\mathcal{M}_{phy,v}$ (Figure 8e), but an increase in \mathcal{M}_{num} (Figure 8f), with over a 50% in \mathcal{M}_{num} for the MPDATA simulation. The HSIMT simulation displayed the opposite trends, with a slight increase in $\mathcal{M}_{phy,v}$, and a slight decrease in \mathcal{M}_{num} .

To summarize, the constant coefficient experiments reaffirm that explicit horizontal mixing reduces numerical mixing (Figure 8f). The time-averaged EKE_n increases for small values of the horizontal mixing coefficients, which we consider to be an improved representation of the ocean state because the submesoscale instabilities are better resolved. While, generally speaking, increased EKE_n does not necessarily correlate with increased model

skill, our experience with this class of idealized models indicates that higher EKE_n is generally aligned with better, more realistic simulations for the regions of parameter space explored here. However, relative levels of EKE_n may not be a suitable metric to assess the representation of submesoscale processes in other models because other numerical errors (i.e., instabilities) can cause energy to accumulate at the grid-scale.

These experiments also suggest numerical mixing behaves different than physical mixing, particularly in frontal zones. In addition, we note that Ilicak et al. (2012) recommended maintaining $Re_\Delta < 10$ to avoid saturating the ocean state with spurious mixing. Our results suggest that $Re_\Delta > 52$ result in a more energetic ocean state (but with higher numerical mixing) compared to the simulations with $Re_\Delta < 10$. A broader discussion of the Re_Δ can be found in Section 5.3.

5. Discussion and Conclusions

5.1. Novelty of the Idealized Model

Previous studies using primitive equation models suggest numerical mixing \mathcal{M}_{num} impacts the larger-scale flow and tracer structure differently than physical mixing \mathcal{M}_{phy} (Fofanova et al., 2021; Henell et al., 2023; Kalra et al., 2019; Kärnä & Baptista, 2016; Ralston et al., 2017). However, most of these studies come with one of the following caveats or challenges: (a) mixing is not quantified directly or online (Fofanova et al., 2021; Kärnä & Baptista, 2016), (b) the domains are highly idealized (Fofanova et al., 2021; Kalra et al., 2019; Mohammadi-Aragh et al., 2015), and (c) quantitative relationships between \mathcal{M}_{num} and model skill in realistic domains requires an extensive array of field observations (Kärnä & Baptista, 2016; Ralston et al., 2017). The current study is novel because we explicitly quantify \mathcal{M}_{num} in an idealized, submesoscale eddy-resolving domain that is able to realize a complex ocean state (Figure 4) that resembles conditions in a realistic simulation of the Texas-Louisiana shelf (Figure 1).

First, we identified and analyzed a base case relative to a case with no wind forcing (Figures 3 and 4). The base case was selected from an ensemble with variable oscillatory, near-inertial wind stress amplitude (Figure A1). While the base case is not fully realistic due to the idealized bathymetry and lack of river forcing, JPDFs of $nFGF$ and $|\mathcal{M}_{num}|$ (Figures 5a and 5b) indicate the sharpening and destruction of horizontal salinity gradients in the base case well-represents the realistic model. The base case also had the maximum ratio of \mathcal{M}_{num} to \mathcal{M}_{phy} (15%) of all the members of the wind ensemble. This choice was intended to make the impacts of \mathcal{M}_{num} easier to identify compared to the no-wind case, because we expected a larger proportion of \mathcal{M}_{num} to \mathcal{M}_{phy} would have had a more quantifiable impact on the ocean state. The idealized domain means that the simulations are computationally inexpensive, enabling us to run a large ensemble of simulations. This domain also allows us to make clear comparisons between ensemble members using an alongshore average.

We quantitatively showed that \mathcal{M}_{num} dominates \mathcal{M}_{phy} in frontal zones due to their sharp horizontal salinity gradients, consistent with previous studies (Holmes et al., 2021; Kalra et al., 2019; Ralston et al., 2017; Wang et al., 2021). Our analysis of $nFGF$ at the ocean surface of both models suggested the strongest \mathcal{M}_{num} occurs in intense regions of frontogenesis and frontolysis. However, frontogenesis produces stronger \mathcal{M}_{num} than frontolysis because the horizontal gradients are actively being sharpened. We also showed that stronger \mathcal{M}_{num} is associated with stronger pointwise horizontal salinity transport (Figures 5c and 5d).

\mathcal{M}_{num} is significant within the mixed layer and dominates at shallow depths where \mathcal{M}_{phy} is weak because of weak vertical tracer gradients. These results suggest modeled mixing processes within frontal zones may be predominantly driven by \mathcal{M}_{num} . Future studies may use our results as a blueprint to investigate the impacts of \mathcal{M}_{num} on specific processes such as symmetric instability (Dong et al., 2021) or the subduction of surface waters due to inertially modulated frontal convergence (Qu, Thomas, Wienkers, et al., 2022).

5.2. The Larger-Scale Impacts of Numerical Mixing

A primary result of our study is that excessive \mathcal{M}_{num} can damp the release of available potential energy APE by suppressing submesoscale baroclinic instabilities. To demonstrate this, we varied \mathcal{M}_{num} in Section 4.2 by varying the tracer advection scheme (MPDATA, U3HC4, and HSIMT), in order to relate an alongshore average state to the magnitude of \mathcal{M}_{num} . This set of simulations did not prescribe any horizontal mixing, so \mathcal{M}_{num} was the only way to dissipate horizontal salinity variance at the grid scale. The simulations are all qualitatively similar across

advection schemes in the sense that they are submesoscale eddy-resolving. However, \mathcal{M}_{num} impacts the larger-scale flow and tracer fields in such a way that simulations with higher \mathcal{M}_{num} have higher integrated available potential energy *APE* and lower eddy kinetic energy *EKE* (Figure 6), indicating the suppression of baroclinic instabilities that release *APE*. Thus, \mathcal{M}_{num} at the submesoscales behaves differently compared to implicit LES models that use artificial numerical dissipation as a way to remove energy at the grid-scale in a downward cascade toward small scales and improve the representation of the solution (Dairay et al., 2017). In other words, though \mathcal{M}_{num} is strongest at the fronts, the submesoscale eddies themselves are altered such that their impact on altering the initial state is reduced.

Our study builds on the findings of Mohammadi-Aragh et al. (2015), who examined the impacts of numerical mixing in the Eady (1949) and Stone (1966) configurations with the General Estuarine Transport Model (Burchard & Bolding, 2002). Their experiments used a zonal, re-entrant, flat-bottom channel with constant meridional and vertical buoyancy gradients for low- and high Rossby number *Ro* flows (*Ro* = 0.1 and 0.8, respectively). They also varied numerical mixing and dissipation by changing the momentum and tracer advection schemes (e.g., MP5, Superbee, WENO), with all schemes (except U3H) different from the ones used in this study. Despite different numerical models and configurations, our studies arrive at a similar conclusion—numerical mixing can suppress baroclinic instabilities and their associated restratification processes.

5.3. Utility of Explicit Horizontal Mixing

The experiments in Section 4.3 (Figure 8) suggest that high-resolution primitive equation models may benefit from employing a small amount of explicit horizontal mixing. In estuarine and coastal modeling, explicit horizontal mixing is often kept as small as possible with the mixing coefficient values determined from tuning experiments. In our model, the benefits manifested as instabilities that are more developed (indicated by higher *EKE*) and a reduction in numerical mixing compared to simulations with no horizontal mixing. We suspect a primary reason numerical mixing impacts processes in frontal zones differently than explicit horizontal mixing is that a significant fraction of grid-scale numerical mixing can be negative due to the anti-diffusive properties of the schemes tested here. The spatial and temporal heterogeneity of this negative mixing makes it difficult to understand precisely how the fronts are affected. Numerical mixing also depends on the flow velocities, whereas explicit horizontal mixing depends only on the magnitude of the horizontal tracer gradients when a constant horizontal diffusivity is used.

These experiments also highlight the difficulties of tuning the horizontal mixing parameterization(s) in ocean models. There are several limitations to our experiment design that should be highlighted for future studies. First, our use of a five to one ratio for horizontal viscosity to diffusivity is somewhat arbitrary. As Griffies and Hallberg (2000) note, it is physically ambiguous as to what the value of the tracer diffusivity should be for a given value of horizontal viscosity. Likewise, the results of the Smagorinsky experiments (Smagorinsky, 1963) were inconclusive across advection schemes and require further exploration. Future studies may find success by pairing a time-dependent horizontal viscosity coefficient with a time-independent diffusion coefficient. The Smagorinsky experiments could also be repeated with a harmonic operator instead of a biharmonic operator.

One metric to assess the amount of horizontal mixing in a simulation is the grid Reynolds number (Griffies & Hallberg, 2000; Ilicak et al., 2012). Ilicak et al. (2012) recommended maintaining a grid Reynolds number $Re_\Delta < 10$ to avoid saturation levels of \mathcal{M}_{num} . The simulations with $Re_\Delta < 10$ featured substantially lower \mathcal{M}_{num} , but at the cost of over-smoothed fronts and suppressed instabilities relative to simulations with no horizontal mixing. Thus, we show that while a smaller Re_Δ is associated with lower \mathcal{M}_{num} , it does not guarantee a more physically realistic ocean state.

We suspect the mismatches in the best choice of Re_Δ between our simulations and previous work could be due to implicit numerical dissipation that is a feature of the U3H momentum advection scheme used in our ROMS simulations. Ilicak et al. (2012) found that ROMS simulations had less spurious diapycnal mixing in several idealized configurations compared to models that used second order momentum schemes for the same values of the Re_Δ . A limitation of using the Re_Δ to characterize the amount of horizontal mixing in a simulation is selecting an appropriate horizontal velocity scale, which has multiple meanings in eddying flows. For example, we could have used a local velocity (similar to Mohammadi-Aragh et al., 2015). However, then it becomes difficult to compare the Re_Δ across simulations with different horizontal viscosity coefficients because the local velocity is spatially and temporally heterogeneous.

5.4. Concerning the Tracer Advection Schemes

A key result of this study is that the HSIMT simulations produced less developed instabilities relative to the MPDATA and U3HC4 simulations regardless of the amount of explicit horizontal mixing added to the simulation (Section 4.2–4.3). Kalra et al. (2019) examined the same advection schemes in a set of simpler idealized configurations, and did not observe excessive \mathcal{M}_{num} in the HSIMT simulations. The underlying reasons for the excessive \mathcal{M}_{num} in the HSIMT simulations for our experiments remains unclear and warrants further investigation.

While the MPDATA and U3HC4 simulations had similar *EKE* and *APE* regardless of whether horizontal mixing was added, U3HC4 exhibited larger \mathcal{M}_{num} than MPDATA across all simulations. We suspect this is because U3HC4 lacks the iterative flux-corrector processes compared to MPDATA. The run times of the HSIMT simulations were 40% faster on average than the MPDATA simulations and 32% faster than the U3HC4 simulations, although the simulations were not optimized for computational efficiency. The relative differences in computational efficiency between these schemes has been suggested previously (Wu, 2023; Wu & Zhu, 2010) but requires more investigation. Since our model is idealized, it is unclear if the trends observed across advection schemes in this study will translate to realistic numerical simulations. More comparative experiments in complex three dimensional domains are needed to determine whether HSIMT generally suffers from excessive numerical mixing.

Appendix A: Near-Inertial Wind Amplitude Ensemble

The impacts of varying the near-inertial alongshore wind stress amplitude τ_0^x on bulk mixing quantities associated with each ensemble member are shown in Figure A1. In addition, we show spatially and temporally averaged parameters related to each mixing quantity to better understand how the bulk mixing quantities change in response to different τ_0^x . To provide a sense of scale for τ_0^x , we plot the amplitude of the wind speed U_{wind} by solving the equation

$$\tau_0^x = \rho_a C_d U_{wind}^2, \quad (\text{A1})$$

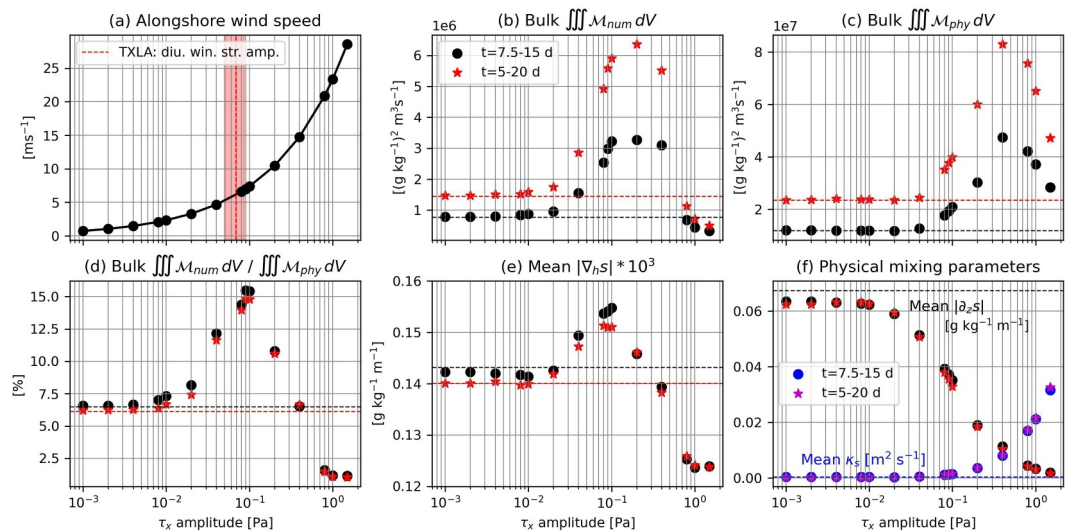


Figure A1. (a) Wind speed as a function of τ_0^x calculated using Equation A1, with each dot representing a different numerical simulation. The amplitude of the diurnal wind stress magnitude spatially and temporally averaged for the entire realistic simulation of the child domain (see Figure 7a of Schlichting et al., 2023) with 95% confidence intervals are shown with the red dashed line and shaded areas. (b) Bulk \mathcal{M}_{num} and (c) \mathcal{M}_{phy} . (d) Ratio of bulk \mathcal{M}_{num} to \mathcal{M}_{phy} expressed as a percent. (e) Spatially and temporally averaged $|\nabla_h s|$. (f) Spatially and temporally averaged $|\partial_z s|$ and κ_v . Quantities in panels (b–f) are calculated in the initially stratified region for two time periods and the horizontal dashed lines show unforced case values for their respective time periods coded by color.

where ρ_a is the density of air and C_d is the drag coefficient set to a constant value of 0.0015. U_{wind} of the ensemble runs span from $<1\text{ m s}^{-1}$ to tropical storm force winds (29 m s^{-1} , until the model blew up).

All bulk quantities are shown from days 5–20 and days 7.5–15 to indicate the trends are robust. The x -axes are on a \log_{10} scale. The time-averaged amplitude of the diurnal (inertial) wind stress magnitude from the realistic model (Figure 7a of Schlichting et al., 2023) is shown to contextualize the base case. The base case wind is slightly more higher than the mean values observed during the realistic simulation. The realistic surface forcing is highly variable, but the spatially averaged wind speed rarely exceeded 10 ms^{-1} .

τ_0^x values from $10^{-3} - 10^{-2}\text{ Pa}$ have little impact on volume-integrated \mathcal{M}_{num} (Figure A1b) or \mathcal{M}_{phy} (Figure A1c). As τ_0^x increases, \mathcal{M}_{num} rapidly grows until plateauing from $\tau_0^x = 0.1\text{--}0.3\text{ Pa}$, then rapidly decreases. In linear space, this qualitatively resembles a Chi-square distribution with few degrees of freedom such that the peak is biased toward zero. The time- and spatially averaged $|\nabla_h s|$ peaks at 0.1 Pa then begins to rapidly decrease (Figure A1e). As the wind stress amplitude approaches 1.0 Pa , winds suppress the instabilities, causing \mathcal{M}_{num} to decrease. For example, strong winds create pulses over the ocean surface (not shown). A background $|\nabla_h s|$ is still maintained because fronts are not allowed to form and there is no explicit horizontal mixing.

Volume-integrated \mathcal{M}_{phy} is more sensitive to the winds relative to \mathcal{M}_{num} . \mathcal{M}_{num} peaks at 0.1 Pa and \mathcal{M}_{phy} peaks at 0.4 Pa . As the near-inertial wind amplitude increases, the instabilities are eventually suppressed while the water column continues to be vertically mixed. The parameters governing \mathcal{M}_{phy} are shown in Figure A1f. The magnitude of the spatially and temporally averaged vertical salinity gradient $|\partial_z s|$ exhibits an inverse sigmoid relationship with τ_0^x (exponential decay in linear space). For ensemble runs with the largest τ_0^x , instabilities are entirely suppressed and wind mixing reduces $|\partial_z s|$ to nil. The mean vertical eddy diffusivity κ_v exhibits exponential growth (linear growth in linear space). The increased growth of \mathcal{M}_{phy} despite the decrease in $|\partial_z s|$ highlights the covariance between κ_v and $|\partial_z s|$.

Data Availability Statement

Analysis of all model output used in this study was done in Python ver 3.9. See Schlichting et al. (2024) for model output, the accompanying analysis code used to make the figures, and materials needed to replicate the idealized numerical simulations.

Acknowledgments

This material is based upon work done in the Study for Exascale Advances in a High-resolution Ocean using ROMS Coupled to E3SM (SEAHORCE) project, supported by the U.S. Department of Energy (DOE), Office of Science, Office of Advanced Scientific Computing Research, and Office of Biological and Environmental Research, Scientific Discovery through Advanced Computing (SciDAC) program. D.S. was funded by NSF grant OCE-1851470. C.S.J. was funded by NSF grant OCE-2219852. R.D.H. was funded by the ICeM project, a U.S. DOE grant. Texas A&M high performance research computing resources were used to produce all numerical simulations. D.S. thanks Ping Chang and John R. Taylor for helpful discussions while preparing this manuscript. We thank Hans Burchard and an anonymous reviewer whose comments improved this manuscript.

References

- Balwada, D., Smith, K. S., & Abernathey, R. (2018). Submesoscale vertical velocities enhance tracer subduction in an idealized Antarctic circumpolar current. *Geophysical Research Letters*, 45(18), 9790–9802. <https://doi.org/10.1029/2018GL079244>
- Balwada, D., Xiao, Q., Smith, S., Abernathey, R., & Gray, A. R. (2021). Vertical fluxes conditioned on vorticity and strain reveal submesoscale ventilation. *Journal of Physical Oceanography*, 51(9), 2883–2901. <https://doi.org/10.1175/JPO-D-21-0016.1>
- Barkan, R., Molemaker, M. J., Srinivasan, K., McWilliams, J. C., & D’Asaro, E. A. (2019). The role of horizontal divergence in submesoscale frontogenesis. *Journal of Physical Oceanography*, 49(6), 1593–1618. <https://doi.org/10.1175/JPO-D-18-0162.1>
- Boccaletti, G., Ferrari, R., & Fox-Kemper, B. (2007). Mixed layer instabilities and restratification. *Journal of Physical Oceanography*, 37(9), 2228–2250. <https://doi.org/10.1175/JPO3101.1>
- Brink, K. (2016). Continental shelf baroclinic instability. Part I: Relaxation from upwelling or downwelling. *Journal of Physical Oceanography*, 46(2), 551–568. <https://doi.org/10.1175/JPO-D-15-0047.1>
- Brink, K., & Seo, H. (2016). Continental shelf baroclinic instability. Part II: Oscillating wind forcing. *Journal of Physical Oceanography*, 46(2), 569–582. <https://doi.org/10.1175/JPO-D-15-0048.1>
- Burchard, H., & Bolding, K. (2002). *Gtcm: A general estuarine transport model: scientific documentation*. Joint Research Centre, Institute for Environment and Sustainability.
- Burchard, H., Lange, X., Klingbeil, K., & MacCready, P. (2019). Mixing estimates for estuaries. *Journal of Physical Oceanography*, 49(2), 631–648. <https://doi.org/10.1175/jpo-d-18-0147.1>
- Burchard, H., & Rennau, H. (2008). Comparative quantification of physically and numerically induced mixing in ocean models. *Ocean Modelling*, 20(3), 293–311. <https://doi.org/10.1016/j.ocemod.2007.10.003>
- Chapman, D. C. (1985). Numerical treatment of cross-shelf open boundaries in a barotropic coastal ocean model. *Journal of Physical Oceanography*, 15(8), 1060–1075. [https://doi.org/10.1175/1520-0485\(1985\)015\(1060:NTOCSO\)2.0.CO;2](https://doi.org/10.1175/1520-0485(1985)015(1060:NTOCSO)2.0.CO;2)
- Cushman-Roisin, B., & Beckers, J.-M. (2011). *Introduction to geophysical fluid dynamics: Physical and numerical aspects*. Academic Press.
- Dairay, T., Lamballais, E., Laizet, S., & Vassilicos, J. C. (2017). Numerical dissipation vs. subgrid-scale modelling for large eddy simulation. *Journal of Computational Physics*, 337, 252–274. <https://doi.org/10.1016/j.jcp.2017.02.035>
- Danilov, S., Sidorenko, D., Wang, Q., & Jung, T. (2017). The finite-volume sea ice–ocean model (fesom2). *Geoscientific Model Development*, 10(2), 765–789. <https://doi.org/10.5194/gmd-10-765-2017>
- de Boyer Montégut, C., Madec, G., Fischer, A. S., Lazar, A., & Iudicone, D. (2004). Mixed layer depth over the global ocean: An examination of profile data and a profile-based climatology. *Journal of Geophysical Research*, 109(C12), C12003. <https://doi.org/10.1029/2004JC002378>
- DiMarco, S. F., Howard, M. K., & Reid, R. O. (2000). Seasonal variation of wind-driven diurnal current cycling on the Texas-louisiana continental shelf. *Geophysical Research Letters*, 27(7), 1017–1020. <https://doi.org/10.1029/1999GL010491>

- Domaradzki, J. A., Xiao, Z., & Smolarkiewicz, P. K. (2003). Effective eddy viscosities in implicit large eddy simulations of turbulent flows. *Physics of Fluids*, 15(12), 3890–3893. <https://doi.org/10.1063/1.1624610>
- Dong, J., Fox-Kemper, B., Zhang, H., & Dong, C. (2021). The scale and activity of symmetric instability estimated from a global submesoscale-permitting ocean model. *Journal of Physical Oceanography*, 51(5), 1655–1670. <https://doi.org/10.1175/jpo-d-20-0159.1>
- Eady, E. T. (1949). Long waves and cyclone waves. *Tellus*, 1(3), 33–52. <https://doi.org/10.3402/tellusa.v1i3.8507>
- Flather, R. (1976). A tidal model of the northwest European continental shelf. *Mem. Soc. Roy. Sci. Liege*, 10, 141–164.
- Fofanova, V., Kärnä, T., Klingbeil, K., Androsov, A., Kuznetsov, I., Sidorenko, D., et al. (2021). Plume spreading test case for coastal ocean models. *Geoscientific Model Development*, 14(11), 6945–6975. <https://doi.org/10.5194/gmd-14-6945-2021.2021>
- Griffies, S. M., & Hallberg, R. W. (2000). Biharmonic friction with a smagorinsky-like viscosity for use in large-scale eddy-permitting ocean models. *Monthly Weather Review*, 128(8), 2935–2946. [https://doi.org/10.1175/1520-0493\(2000\)128\(2935:BFWASL\)2.0.CO;2](https://doi.org/10.1175/1520-0493(2000)128(2935:BFWASL)2.0.CO;2)
- Griffies, S. M., Pacanowski, R. C., & Hallberg, R. W. (2000). Spurious diapycnal mixing associated with advection in a z-coordinate ocean model. *Monthly Weather Review*, 128(3), 538–564. [https://doi.org/10.1175/1520-0493\(2000\)128\(0538:sdmawa\)2.0.co;2](https://doi.org/10.1175/1520-0493(2000)128(0538:sdmawa)2.0.co;2)
- Grinstein, F. F., Margolin, L. G., & Rider, W. J. (2007). *Implicit large eddy simulation* (Vol. 10). Cambridge university press Cambridge.
- Hedström, K. S. (2009). Technical manual for a coupled sea-ice/ocean circulation model (version 1). *Minerals Management Service*.
- Henell, E., Burchard, H., Gräwe, U., & Klingbeil, K. (2023). Spatial composition of the diahaline overturning circulation in a fjord-type, non-tidal estuarine system. *Journal of Geophysical Research: Oceans*, 128(12), e2023JC019862. <https://doi.org/10.1029/2023JC019862>
- Hetland, R. D. (2017). Suppression of baroclinic instabilities in buoyancy-driven flow over sloping bathymetry. *Journal of Physical Oceanography*, 47(1), 49–68. <https://doi.org/10.1175/jpo-d-15-0240.1>
- Holmes, R. M., Zika, J. D., Griffies, S. M., Hogg, A. M., Kiss, A. E., & England, M. H. (2021). The geography of numerical mixing in a suite of global ocean models. *Journal of Advances in Modeling Earth Systems*, 13(7), e2020MS002333. <https://doi.org/10.1029/2020MS002333>
- Hoskins, B. J. (1982). The mathematical theory of frontogenesis. *Annual Review of Fluid Mechanics*, 14(1), 131–151. <https://doi.org/10.1146/annurev.fl.14.010182.001023>
- Ilicak, M. (2016). Quantifying spatial distribution of spurious mixing in ocean models. *Ocean Modelling*, 108, 30–38. <https://doi.org/10.1016/j.ocemod.2016.11.002>
- Ilicak, M., Adcroft, A. J., Griffies, S. M., & Hallberg, R. W. (2012). Spurious dianeutral mixing and the role of momentum closure. *Ocean Modelling*, 45, 37–58. <https://doi.org/10.1016/j.ocemod.2011.10.003>
- Kalra, T. S., Li, X., Warner, J. C., Geyer, W. R., & Wu, H. (2019). Comparison of physical to numerical mixing with different tracer advection schemes in estuarine environments. *Journal of Marine Science and Engineering*, 7(10), 338. <https://doi.org/10.3390/jmse710038>
- Kärnä, T., & Baptista, A. M. (2016). Evaluation of a long-term hindcast simulation for the Columbia River estuary. *Ocean Modelling*, 99, 1–14. <https://doi.org/10.1016/j.ocemod.2015.12.007>
- Klingbeil, K., Mohammadi-Aragh, M., Gräwe, U., & Burchard, H. (2014). Quantification of spurious dissipation and mixing-discrete variance decay in a finite-volume framework. *Ocean Modelling*, 81, 49–64. <https://doi.org/10.1016/j.ocemod.2014.06.001>
- Kobashi, D., & Hetland, R. (2020). Reproducibility and variability of submesoscale frontal eddies on a broad, low-energy shelf of freshwater influence. *Ocean Dynamics*, 70(11), 1377–1395. <https://doi.org/10.1007/s10236-020-01401-4>
- Lemarié, F., Debreu, L., Madec, G., Demange, J., Molines, J.-M., & Honnorat, M. (2015). Stability constraints for oceanic numerical models: Implications for the formulation of time and space discretizations. *Ocean Modelling*, 92, 124–148. <https://doi.org/10.1016/j.ocemod.2015.06.006>
- Leonard, B., MacVean, M., & Lock, A. (1993). Positivity-preserving numerical schemes for multidimensional advection Tech. Rep. NASA.
- Li, X., Geyer, W. R., Zhu, J., & Wu, H. (2018). The transformation of salinity variance: A new approach to quantifying the influence of straining and mixing on estuarine stratification. *Journal of Physical Oceanography*, 48(3), 607–623. <https://doi.org/10.1175/jpo-d-17-0189.1>
- MacCready, P., Geyer, W. R., & Burchard, H. (2018). Estuarine exchange flow is related to mixing through the salinity variance budget. *Journal of Physical Oceanography*, 48(6), 1375–1384. <https://doi.org/10.1175/jpo-d-17-0266.1>
- Marchesiello, P., Debreu, L., & Couvelard, X. (2009). Spurious diapycnal mixing in terrain-following coordinate models: The problem and a solution. *Ocean Modelling*, 26(3–4), 156–169. <https://doi.org/10.1016/j.ocemod.2008.09.004>
- McWilliams, J. C. (2016). Submesoscale currents in the ocean. *Proceedings of the Royal Society A: Mathematical, Physical and Engineering Sciences*, 472(2189), 20160117. <https://doi.org/10.1098/rspa.2016.0117>
- McWilliams, J. C. (2019). A survey of submesoscale currents. *Geoscience Letters*, 6(1), 1–15. <https://doi.org/10.1186/s40562-019-0133-3>
- McWilliams, J. C. (2021). Oceanic frontogenesis. *Annual Review of Marine Science*, 13(1), 227–253. <https://doi.org/10.1146/annurev-marine-032320-120725>
- Megann, A. (2018). Estimating the numerical diapycnal mixing in an eddy-permitting ocean model. *Ocean Modelling*, 121, 19–33. <https://doi.org/10.1016/j.ocemod.2017.11.001>
- Megann, A., Chanut, J., & Storkey, D. (2022). Assessment of the z time-filtered arbitrary Lagrangian-Eulerian coordinate in a global eddy-permitting ocean model. *Journal of Advances in Modeling Earth Systems*, 14(11), e2022MS003056. <https://doi.org/10.1029/2022MS003056>
- Megann, A., & Storkey, D. (2021). Exploring viscosity space in an eddy-permitting global ocean model: Is viscosity a useful control for numerical mixing? *Journal of Advances in Modeling Earth Systems*, 13(5), e2020MS002263. <https://doi.org/10.1029/2020MS002263>
- Mohammadi-Aragh, M., Klingbeil, K., Brügmann, N., Eden, C., & Burchard, H. (2015). The impact of advection schemes on restratification due to lateral shear and baroclinic instabilities. *Ocean Modelling*, 94, 112–127. <https://doi.org/10.1016/j.ocemod.2015.07.021>
- Qu, L., Thomas, L. N., Hetland, R. D., & Kobashi, D. (2022a). Mixing driven by critical reflection of near-inertial waves over the Texas-Louisiana shelf. *Journal of Physical Oceanography*, 52(11), 2891–2906. <https://doi.org/10.1175/jpo-d-22-0004.1>
- Qu, L., Thomas, L. N., Wienkers, A. F., Hetland, R. D., Kobashi, D., Taylor, J. R., et al. (2022b). Rapid vertical exchange at fronts in the northern Gulf of Mexico. *Nature Communications*, 13(1), 1–11. <https://doi.org/10.1038/s41467-022-33251-7>
- Ralston, D. K., Cowles, G. W., Geyer, W. R., & Holleman, R. C. (2017). Turbulent and numerical mixing in a salt wedge estuary: Dependence on grid resolution, bottom roughness, and turbulence closure. *Journal of Geophysical Research: Oceans*, 122(1), 692–712. <https://doi.org/10.1002/2016jc011738>
- Redi, M. H. (1982). Oceanic isopycnal mixing by coordinate rotation. *Journal of Physical Oceanography*, 12(10), 1154–1158. [https://doi.org/10.1175/1520-0485\(1982\)012\(1154:OIMBCR\)2.0.CO;2](https://doi.org/10.1175/1520-0485(1982)012(1154:OIMBCR)2.0.CO;2)
- Rennau, H., & Burchard, H. (2009). Quantitative analysis of numerically induced mixing in a coastal model application. *Ocean Dynamics*, 59(5), 671–687. <https://doi.org/10.1007/s10236-009-0201-x>
- Roman, F., Stipech, G., Armenio, V., Inghilesi, R., & Corsini, S. (2010). Large eddy simulation of mixing in coastal areas. *International Journal of Heat and Fluid Flow*, 31(3), 327–341. <https://doi.org/10.1016/j.ijheatfluidflow.2010.02.000>

- Ruiz, S., Claret, M., Pascual, A., Olita, A., Troupin, C., Capet, A., et al. (2019). Effects of oceanic mesoscale and submesoscale frontal processes on the vertical transport of phytoplankton. *Journal of Geophysical Research: Oceans*, 124(8), 5999–6014. <https://doi.org/10.1029/2019JC015034>
- Schllichting, D., Hetland, R., & Jones, C. S. (2024). Analysis code and figure data for “Numerical mixing suppresses submesoscale baroclinic instabilities over sloping bathymetry. *Zenodo*. <https://doi.org/10.5281/zenodo.10735282>
- Schllichting, D., Qu, L., Kobashi, D., & Hetland, R. (2023). Quantification of physical and numerical mixing in a coastal ocean model using salinity variance budgets. *Journal of Advances in Modeling Earth Systems*, 15(4), e2022MS003380. <https://doi.org/10.1029/2022MS003380>
- Shchepetkin, A. F., & McWilliams, J. C. (1998). Quasi-monotone advection schemes based on explicit locally adaptive dissipation. *Monthly Weather Review*, 126(6), 1541–1580. [https://doi.org/10.1175/1520-0493\(1998\)126\(1541:QMASBO\)2.0.CO;2](https://doi.org/10.1175/1520-0493(1998)126(1541:QMASBO)2.0.CO;2)
- Shchepetkin, A. F., & McWilliams, J. C. (2005). The regional oceanic modeling system (ROMS): A split-explicit, free-surface, topography-following-coordinate oceanic model. *Ocean Modelling*, 9(4), 347–404. <https://doi.org/10.1016/j.ocemod.2004.08.002>
- Shchepetkin, A. F., & McWilliams, J. C. (2009). Computational kernel algorithms for fine-scale, multiprocess, longtime oceanic simulations. In *Handbook of numerical analysis* (Vol. 14, pp. 121–183). Elsevier. [https://doi.org/10.1016/S1570-8659\(08\)01202-0](https://doi.org/10.1016/S1570-8659(08)01202-0)
- Simpson, J. H., Brown, J., Matthews, J., & Allen, G. (1990). Tidal straining, density currents, and stirring in the control of estuarine stratification. *Estuaries*, 13(2), 125–132. <https://doi.org/10.2307/1351581>
- Smagorinsky, J. (1963). General circulation experiments with the primitive equations: I. The basic experiment. *Monthly Weather Review*, 91(3), 99–164. [https://doi.org/10.1175/1520-0493\(1963\)091<0099:gcewtp>2.3.co;2](https://doi.org/10.1175/1520-0493(1963)091<0099:gcewtp>2.3.co;2)
- Smolarkiewicz, P. K. (1984). A fully multidimensional positive definite advection transport algorithm with small implicit diffusion. *Journal of Computational Physics*, 54(2), 325–362. [https://doi.org/10.1016/0021-9991\(84\)90121-9](https://doi.org/10.1016/0021-9991(84)90121-9)
- Smolarkiewicz, P. K., & Margolin, L. G. (1998). Mpdata: A finite-difference solver for geophysical flows. *Journal of Computational Physics*, 140(2), 459–480. <https://doi.org/10.1006/jcph.1998.5901>
- Stone, P. H. (1966). On non-geostrophic baroclinic stability. *Journal of the Atmospheric Sciences*, 23(4), 390–400. [https://doi.org/10.1175/1520-0469\(1966\)023<0390:ONGBS>2.0.CO;2](https://doi.org/10.1175/1520-0469(1966)023<0390:ONGBS>2.0.CO;2)
- Su, Z., Wang, J., Klein, P., Thompson, A. F., & Menemenlis, D. (2018). Ocean submesoscales as a key component of the global heat budget. *Nature Communications*, 9(1), 775. <https://doi.org/10.1038/s41467-018-02983-w>
- Sweby, P. K. (1984). High resolution schemes using flux limiters for hyperbolic conservation laws. *SIAM Journal on Numerical Analysis*, 21(5), 995–1011. <https://doi.org/10.1137/0721062>
- Taylor, J. R., & Thompson, A. F. (2023). Submesoscale dynamics in the upper ocean. *Annual Review of Fluid Mechanics*, 55(1), 103–127. <https://doi.org/10.1146/annurev-fluid-031422-095147>
- Thomson, R. E., & Fine, I. V. (2003). Estimating mixed layer depth from oceanic profile data. *Journal of Atmospheric and Oceanic Technology*, 20(2), 319–329. [https://doi.org/10.1175/1520-0426\(2003\)020<0319:emldfo>2.0.co;2](https://doi.org/10.1175/1520-0426(2003)020<0319:emldfo>2.0.co;2)
- Thornber, B., Mosedale, A., & Drikakis, D. (2007). On the implicit large eddy simulations of homogeneous decaying turbulence. *Journal of Computational Physics*, 226(2), 1902–1929. <https://doi.org/10.1016/j.jcp.2007.06.030>
- Umlauf, L., & Burchard, H. (2003). A generic length-scale equation for geophysical turbulence models. *Journal of Marine Research*, 61(2), 235–265. <https://doi.org/10.1357/002224003322005087>
- Veronis, G. (1975). The role of models in tracer studies. *Numerical models of ocean circulation*, 133–146.
- Wang, T., & Geyer, W. R. (2018). The balance of salinity variance in a partially stratified estuary: Implications for exchange flow, mixing, and stratification. *Journal of Physical Oceanography*, 48(12), 2887–2899. <https://doi.org/10.1175/jpo-d-18-0032.1>
- Wang, T., Wei, Z., Jiang, W., Xu, T., Chen, J.-L., & Bian, C. (2021). Quantification of numerical mixing in coastal ocean models through an offline method. *Ocean Engineering*, 222, 108588. <https://doi.org/10.1016/j.oceaneng.2021.108588>
- Warner, J. C., Armstrong, B., He, R., & Zambon, J. B. (2010). Development of a coupled ocean-atmosphere-wave-sediment transport (COAWST) modeling system. *Ocean Modelling*, 35(3), 230–244. <https://doi.org/10.1016/j.ocemod.2010.07.010>
- Warner, J. C., Geyer, W. R., Ralston, D. K., & Kalra, T. (2020). Using tracer variance decay to quantify variability of salinity mixing in the Hudson River estuary. *Journal of Geophysical Research: Oceans*, 125(12), e2020JC016096. <https://doi.org/10.1029/2020JC016096>
- Warner, J. C., Sherwood, C. R., Arango, H. G., & Signell, R. P. (2005). Performance of four turbulence closure models implemented using a generic length scale method. *Ocean Modelling*, 8(1–2), 81–113. <https://doi.org/10.1016/j.ocemod.2003.12.003>
- Waruszewski, M., Kühnlein, C., Pawłowska, H., & Smolarkiewicz, P. K. (2018). Mpdata: Third-order accuracy for variable flows. *Journal of Computational Physics*, 359, 361–379. <https://doi.org/10.1016/j.jcp.2018.01.005>
- Wu, H. (2023). Evaluation on the tracer simulation under different advection schemes in the ocean model. *Anthropocene Coasts*, 6(1), 1. <https://doi.org/10.1007/s44218-023-00017-7>
- Wu, H., & Zhu, J. (2010). Advection scheme with 3rd high-order spatial interpolation at the middle temporal level and its application to saltwater intrusion in the changjiang estuary. *Ocean Modelling*, 33(1–2), 33–51. <https://doi.org/10.1016/j.ocemod.2009.12.001>
- Zhang, W., & Hetland, R. D. (2018). A study of baroclinic instability induced convergence near the bottom using water age simulations. *Journal of Geophysical Research: Oceans*, 123(3), 1962–1977. <https://doi.org/10.1002/2017JC013561>